

Nonlinear Combustion Instability in
Liquid-Propellant Rocket Motors

Samuel Z. Burstein and Wallace Chinitz

Second Quarterly Report
to
Jet Propulsion Laboratory

January 30, 1968

JPL CONTRACT 951946

"This work was performed for the Jet Propulsion Laboratory, California Institute of Technology, as sponsored by the National Aeronautics and Space Administration under Contract NAS7-100."

"This report contains information prepared by Mathematical Applications Group, Inc. (MAGI) under JPL subcontract. Its content is not necessarily endorsed by the Jet Propulsion Laboratory, California Institute of Technology, or the National Aeronautics and Space Administration."

TABLE OF CONTENTS

INTRODUCTION.....	1
DROPLET EVAPORATION AND COMBUSTION ANALYSES.....	2
A. The Rate of the $\text{N}_2\text{H}_4/\text{N}_2\text{O}_4$ Reaction.....	2
B. The Diffusion-Controlled Flame Analysis.....	11
FLUID DYNAMIC MODEL.....	17
A. First-Row Mesh Point Calculation.....	17
B. An Exact Solution-Comparison with Machine Experiment.....	19
C. A Finite Amplitude Calculation of a Rotating Wave.....	21
D. Convergence of the Difference Equations.....	23
E. Simple Forcing Function.....	26
F. Program COMB Status.....	28

INTRODUCTION

During the second quarter of the contract there has been significant progress in the construction of a mathematical model describing the dynamics of a rotating finite-amplitude wave in a cylindrical combustion chamber. This quarterly report describes some of the details of this activity.

The first section describes the theory of finite rate processes in the combustion of hydrazine (N_2H_4)/nitrogen tetroxide (N_2O_4); the results will be used to predict kinetic parameters for the modified surface flame model of combustion. Also discussed in this section are some results obtained from the diffusion flame analysis.

The second section is involved with the fluid dynamic model. A new treatment for the calculation of special mesh points in COMB is presented. Most important, however, the results of some time dependent computations are described in which a finite amplitude pressure wave is allowed to rotate and steepen in a cylindrical chamber. The reader should refer to reference 1 for background material and additional references (especially reference 20).

The authors would like to acknowledge the significant contribution of Harold Schechter in the organization, analysis and programming of the digital programs being developed in this research program.

I. THE DROPLET EVAPORATION AND COMBUSTION ANALYSES

A. The Rate of the N_2H_4/N_2O_4 Reaction

It will be recalled (Ref. 1) that the species conservation equation including finite rate chemical reaction can be written:

$$a \frac{dY_i}{d\eta} - \frac{d}{d\eta} \left(\eta^2 \frac{dY_i}{d\eta} \right) = - i_i \eta^2 b Y_F^{N_F} Y_O^{N_O} \quad (1)$$

where a = the dimensionless mass burning rate

Y_i = mass fraction of species i

η = radius/droplet radius

$i_i = M_i(\rho)^{N_F+N_O-1} / M_F^{N_F} M_O^{N_O}$

M_i = molecular weight of species i

ρ = mass density

N_F, N_O = reaction orders

$b = r_D^2 k / D$

k = Arrhenius reaction rate constant = $A(T) \exp(-E/RT)$

D = diffusion coefficient

It was also shown (Ref. 1) that by neglecting the energy transport due to concentration gradients (the Dufour effect) and assuming the Lewis number to be unity, the energy equation takes on the same form as equation (1) above:

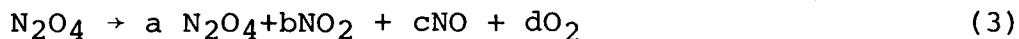
$$a \frac{dt}{d\eta} - \frac{d}{d\eta} \left(\eta^2 \frac{dt}{d\eta} \right) = - i_F \eta^2 b Y_F^{N_F} Y_O^{N_O} \quad (2)$$

where $t \equiv (T - T_\infty) / (Q/c_p)$.

In order to apply Peskin's (Ref. 2) modified flame surface analysis, realistic estimates must be obtained for the reaction rate constant, $k = A(T)\exp(-E/RT)$, and the reaction orders, N_F and N_O , corresponding to the N_2H_4/N_2O_4 reaction. These can be obtained from a one-dimensional, finite-rate analysis of the oxidation process, using the simplified chemical kinetic mechanism deduced from Sawyer, and discussed in Ref. 1. This method is formulated in the following manner.

As mentioned above, the flow equations are written for one-dimensional, constant pressure, inviscid flow along streamtubes, with the following additional assumptions:

- a. Negligible diffusion normal to the flow direction, leading to a uniform mixture of (gaseous) species at any streamwise point. Therefore, the oxidation is taken to be 'reaction-controlled'.
- b. The flow is steady and adiabatic.
- c. The initial concentrations of the oxidizing species are obtained in accordance with the following reaction equation and with the assumption of chemical equilibrium:



The method for obtaining the equilibrium species concentrations is detailed in Appendix A.

With these assumptions, the relevant equations are:

Energy Conservation

$$\frac{dh}{dt} = 0 ; h = \text{constant} \quad (4)$$

where h includes sensible and chemical enthalpy.

Species Conservation

$$\rho \frac{dy_i}{dt} = r_i \quad (5)$$

Equation of State

$$\rho = \frac{pM}{RT} \quad (6)$$

Auxiliary Equations

$$h = \sum_i Y_i h_i \quad (7)$$

$$M = \left(\sum_i \frac{Y_i}{M_i} \right)^{-1} \quad (8)$$

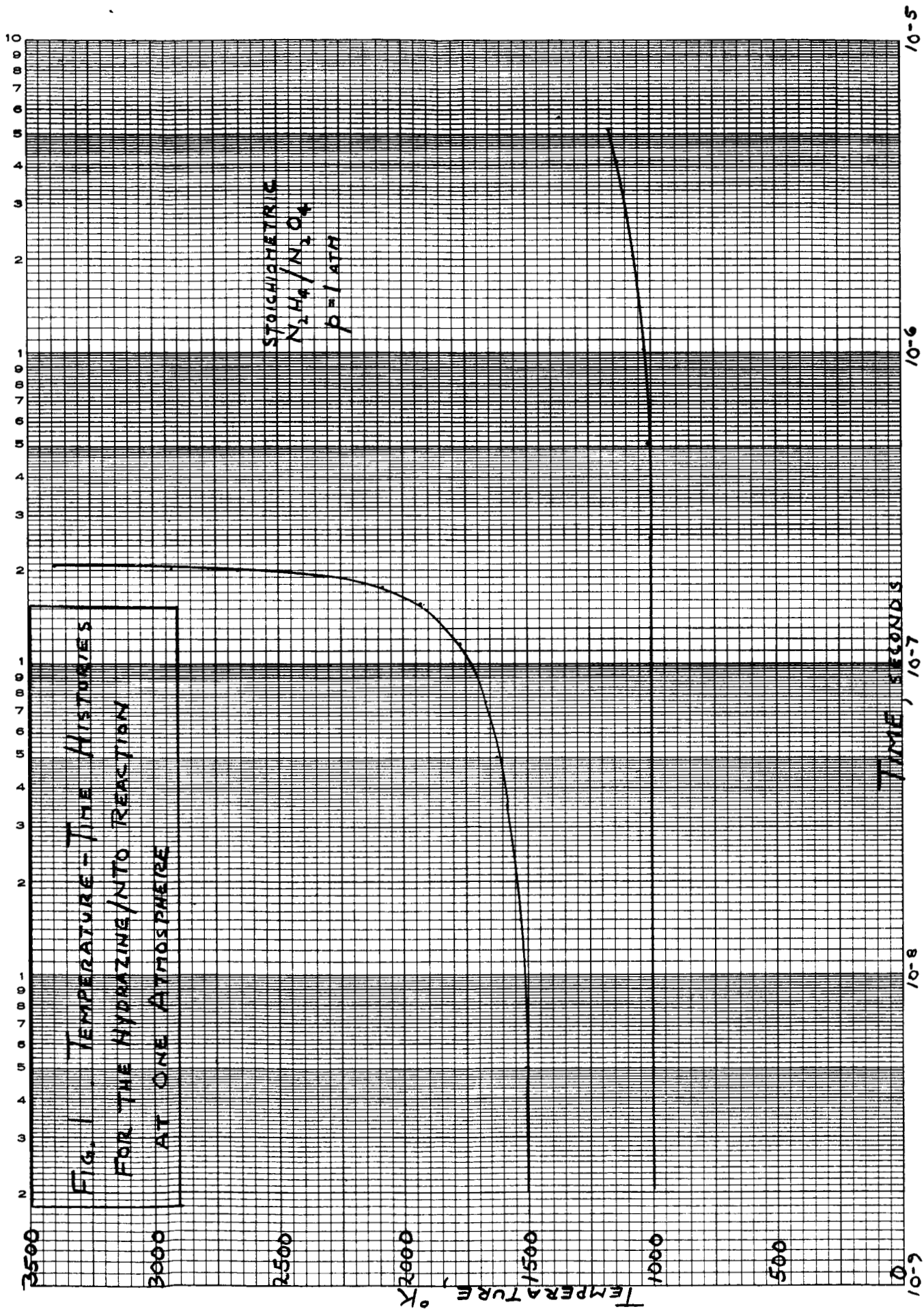
The enthalpy terms are taken to be linear in form:

$$h_i = \Delta_i + \bar{c}_{p_i} (T - T_{REF}) \quad (9)$$

where the reference temperature was chosen to be 1000°K. Values for Δ_i and \bar{c}_{p_i} were obtained from the data of Reference 5. The chemical kinetic mechanism and the species generation terms, r_i , are in Tables I and II, respectively. The reaction rate constants are in Table I.

It should be emphasized that this premixed, homogeneous gas-phase analysis is designed to supply an appropriate representation of the overall (global) oxidation reaction rate, for use in equations (1) and (2). It is not, of course, a representation of the processes occurring around the fuel drop, where a counter-flow diffusion flame exists, as described by equations (1) and (2).

Results for two values of the ambient pressure are shown in Figures 1 and 2. At one atmosphere (Figure 1), and an initial temperature of 1500°K, the reaction is seen to commence at about 10^{-8} seconds, continue smoothly until about 10^{-7} seconds after



which a rapid rise in temperature is noted. If the calculations were continued, a rapid leveling off to the adiabatic flame temperature would be noted. In this case, the ignition delay time can be estimated to be 10^{-7} seconds.

At the lower initial temperature ($T_i = 1000^\circ\text{K}$), the ignition delay time is seen to increase in Figure 1 to about 5×10^{-6} seconds.

When the pressure is increased to 20 atmospheres (Figure 2), a somewhat different behavior is noted. At both initial temperatures, the reaction is seen to commence quite early (at about 10^{-9} seconds for $T_i = 1500^\circ\text{K}$, and before 10^{-7} seconds for $T_i = 1000^\circ\text{K}$). However, a pause in the reaction then occurs and, for the case of $T_i = 1500^\circ\text{K}$, between 5×10^{-9} and 5×10^{-8} seconds little temperature change is noted. After 5×10^{-8} seconds, a smooth and, ultimately, rapid rise in temperature is noted.

The reason for this behavior can be explained by reference to Figure 3 and Table II. In Figure 3, it is seen that NO_2 disappears rapidly during this initial temperature rise, with a corresponding decrease in the concentration of hydrazine. This same behavior was not noted for the case of $p = 1$ atm because reaction number 2 in Table II is second-order and, hence, predominates at higher pressures. An accompanying increase of NO , as a result of reaction 2, can be seen in Figure 3 as well.

After the depletion of the NO_2 , the $\text{N}_2\text{H}_4/\text{NO}$ and $\text{N}_2\text{H}_4/\text{O}_2$ oxidation reactions take over and proceed as first-order reactions (Table II), leading to a second 'delay' period, and a subsequent rapid reaction at about 10^{-7} seconds. The behavior of NH_3 and

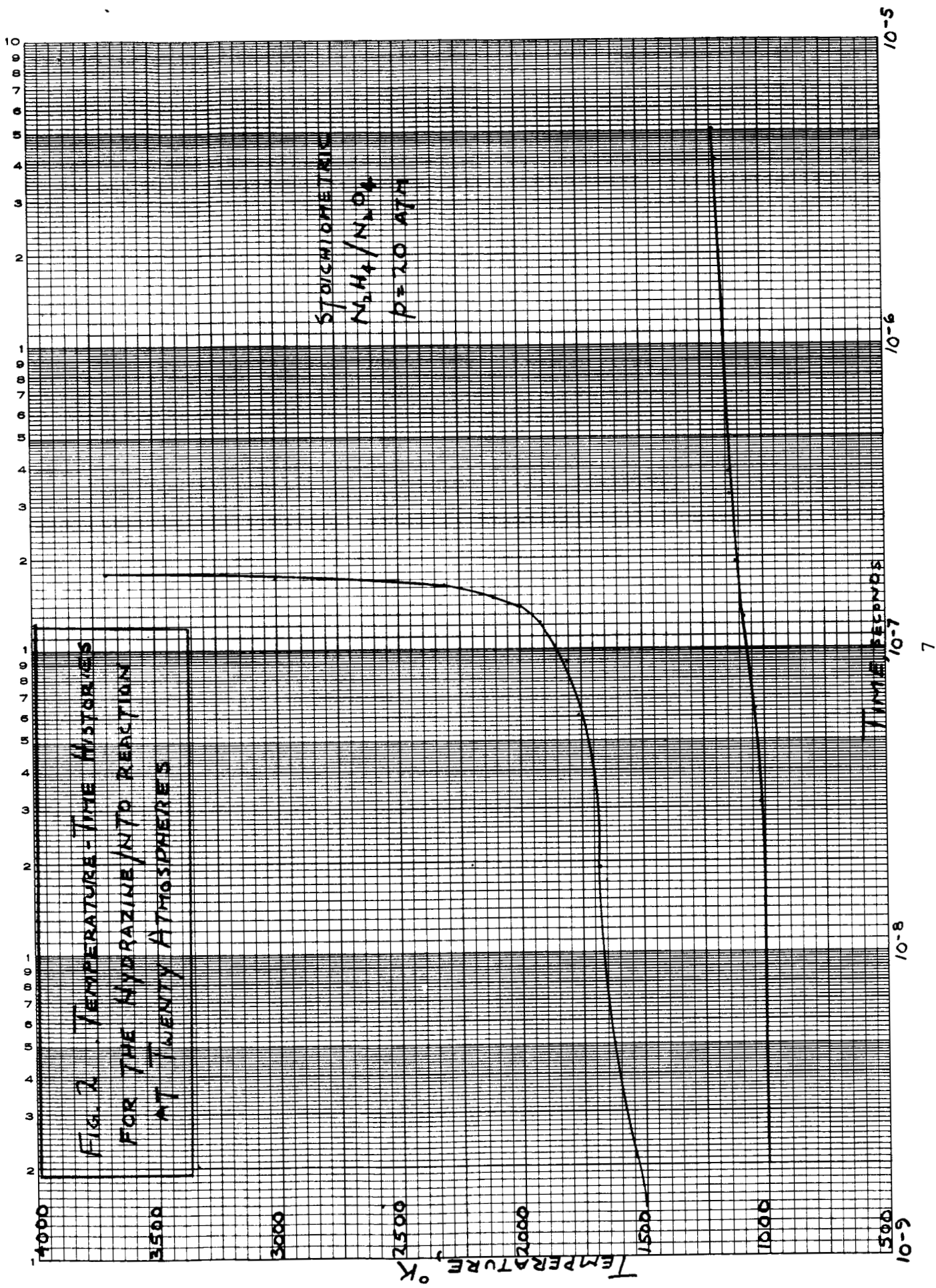
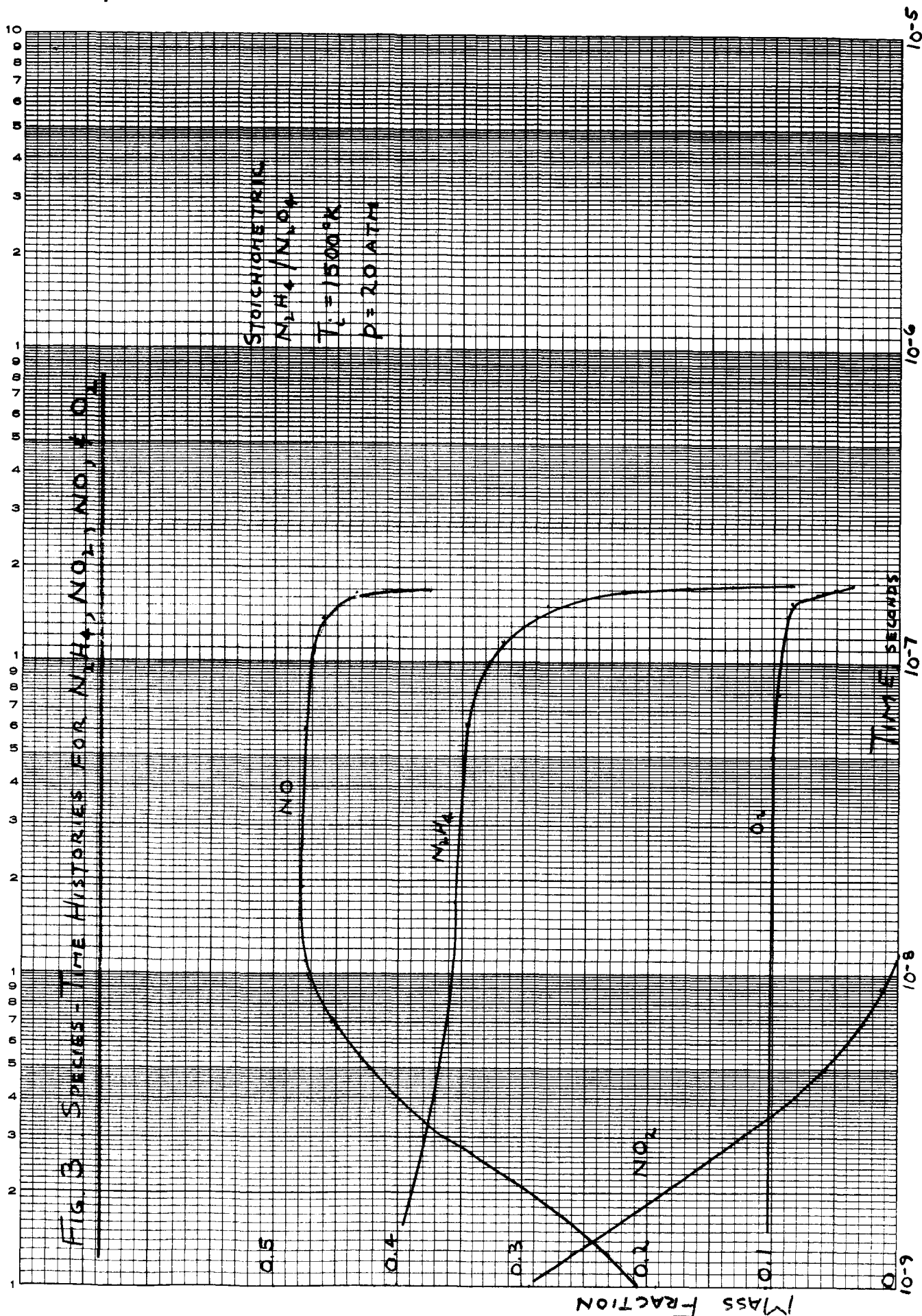


FIG. 3 SPECIES-TIME HISTORIES FOR N_2H_4 , NO , NO_2 , NO , & O_2

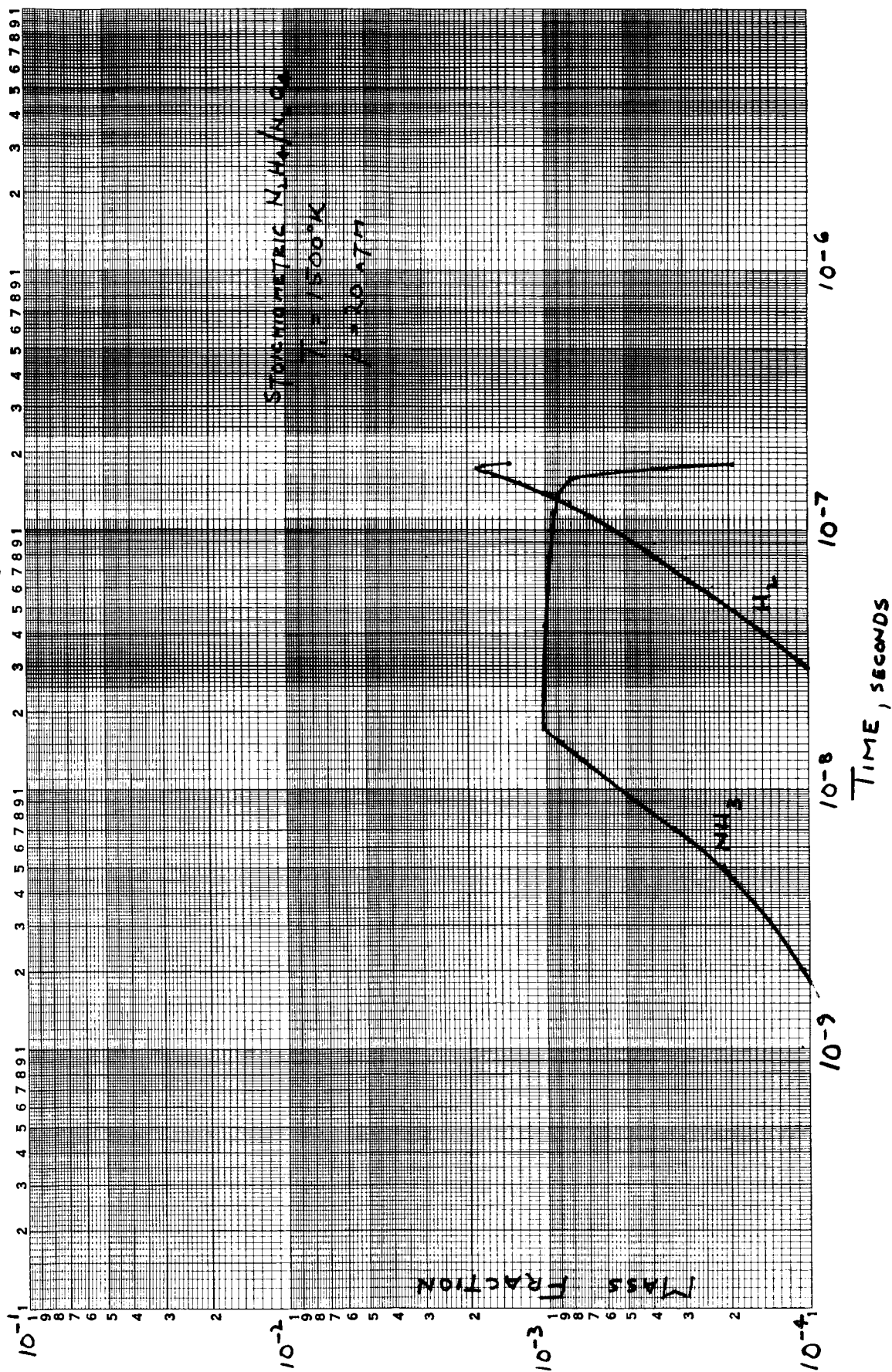
STOICHIOMETRIC
 N_2H_4 / N_2O_4
 $T_c = 1500^\circ K$
 $p = 20 \text{ ATM}$



H_2 is shown in Figure 4. It can be seen that they rise in concentration initially, as a consequence of the hydrazine decomposition reaction (reaction 1, Table II), then rapidly disappear when the main reaction occurs.

It is clear then, that the 'ignition delay time' is difficult to define in the pressure regime where this two-step reaction occurs. It can be anticipated that the traditional plot of ignition delay as a function of reciprocal temperature will not produce a straight line since the rate-controlling reactions are different at different pressures. This will lead to the requirement for a different 'global' reaction rate constant for the high and low pressure regimes. Current efforts are directed toward obtaining sufficient computer runs so that the chemical kinetic parameters can be determined in both pressure regimes.

FIGURE 4. SPECIES-TIME HISTORIES FOR NH_3 & H_2



B. The Diffusion-Controlled Flame Analysis

The diffusion-controlled flame analysis which was described in Reference 1 has been coupled to the basic computer program COMB. In this section, we compare the results obtained from this analysis with those obtained from a more elaborate analysis which has been published in the literature, as well with some experimental results.

It will be recalled that the modified Godsave equation developed in Reference 1 was

$$\dot{m}_F^O = \frac{2\pi d_L k}{c_p} \ln \left[1 + \frac{c_p (T_\infty - T_2) + (Y_{O,\infty}) (\phi f_s \Delta H_R)}{L_F} \right] \quad (3)$$

where \dot{m}_F^O = mass burning rate in stagnant surroundings

d_L = droplet diameter

k = fuel thermal conductivity

c_p = fuel specific heat

T_∞ = ambient temperature

T_L = saturation temperature of the fuel
droplet at the chamber pressure

$Y_{O,\infty}$ = ambient mass fraction of oxidizer

ϕ = fuel-oxidant equivalence ratio

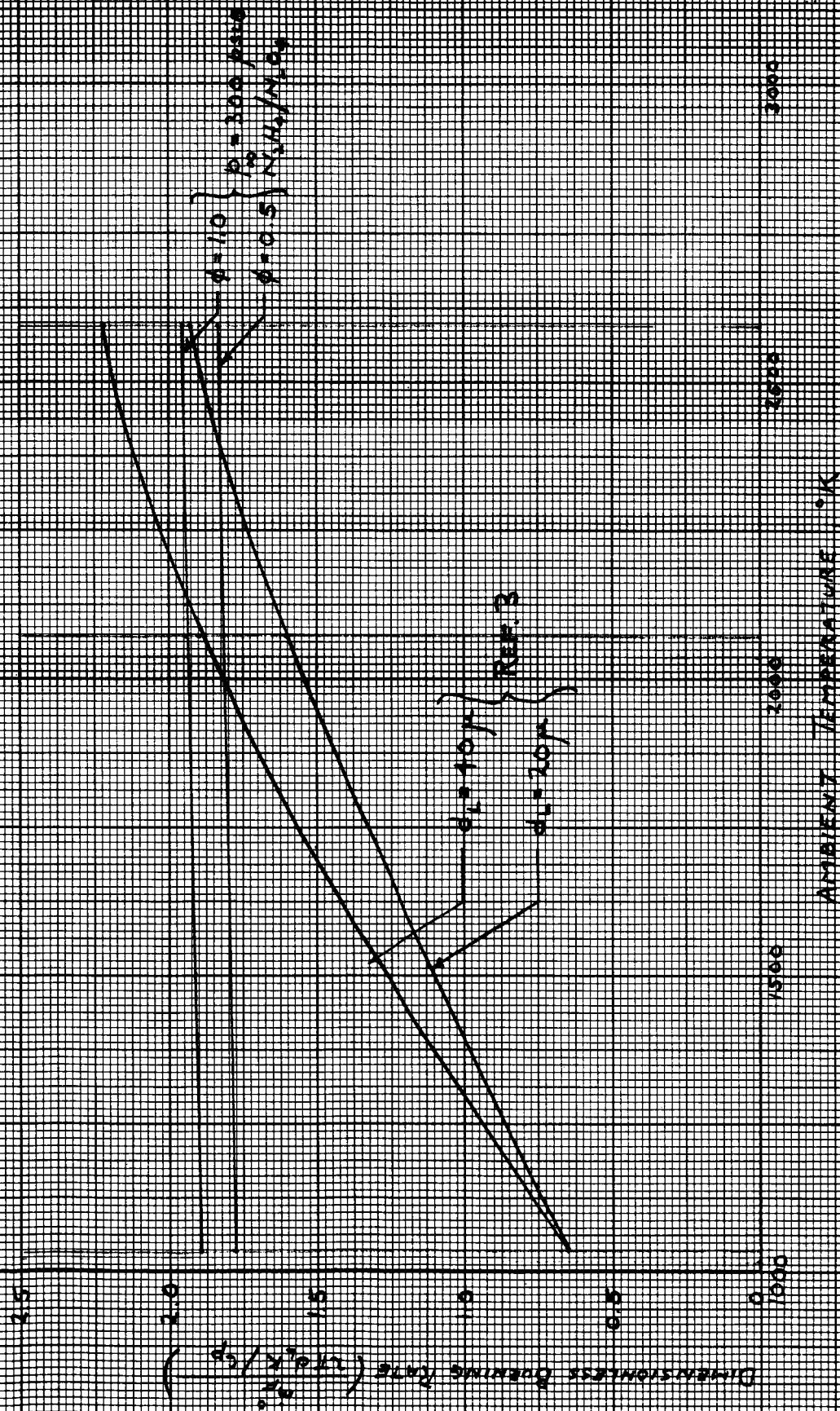
f_s = stoichiometric fuel-oxidant ratio

ΔH_R = heat of reaction of the mixture

L_F = latent heat of the fuel

Figure 5 shows the results of the solution of equation (3) in terms of the dimensionless burning rate, $W \equiv \dot{m}_F^O / (2\pi d_L k / c_p)$, for

FIGURE 3. Comparison of Dimensionless Burning Rate with the Data of Reference



two values of equivalence ratio and 300 psia chamber pressure. The curves of W are virtually straight lines, and are nearly independent of T_∞ . These results are, of course, for the N_2H_4/N_2O_4 system.

Also shown are the theoretical results of Reference 3. Strictly speaking, these results are not directly comparable with those presented herein since they are apparently for hydrazine decomposition (in the absence of N_2O_4) and, probably, at one atmosphere. Of principle interest, however, are the facts that the orders-of-magnitude are the same, but that the results of Reference 3 indicate a much greater dependence of W on the ambient temperature. This stems principally from the fact that the analysis of Reference 3 includes a finite-rate reaction term (taken to be first-order) which is sensitive to the ambient temperature. The modified flame-sheet analysis being developed under this program contains a finite-rate reaction term as well, and can be expected to show a like dependence on T_∞ .

Perhaps a more apt comparison is that shown in Figure 6. The results obtained from equation (3) are compared with some experimental results obtained from Reference 4. These latter results are presumably at one atmosphere, but the ambient temperature is not specified in Reference 4. As can be seen, equation (3) predicts the mass burning rate reasonably well and, of course, predicts the linear variation of \dot{m}_F^0 with d_L .

The effects of the three variables T_∞ , p_∞ , and ϕ on W are summarized in Figure 7. As can be seen, (a) reducing the equivalence

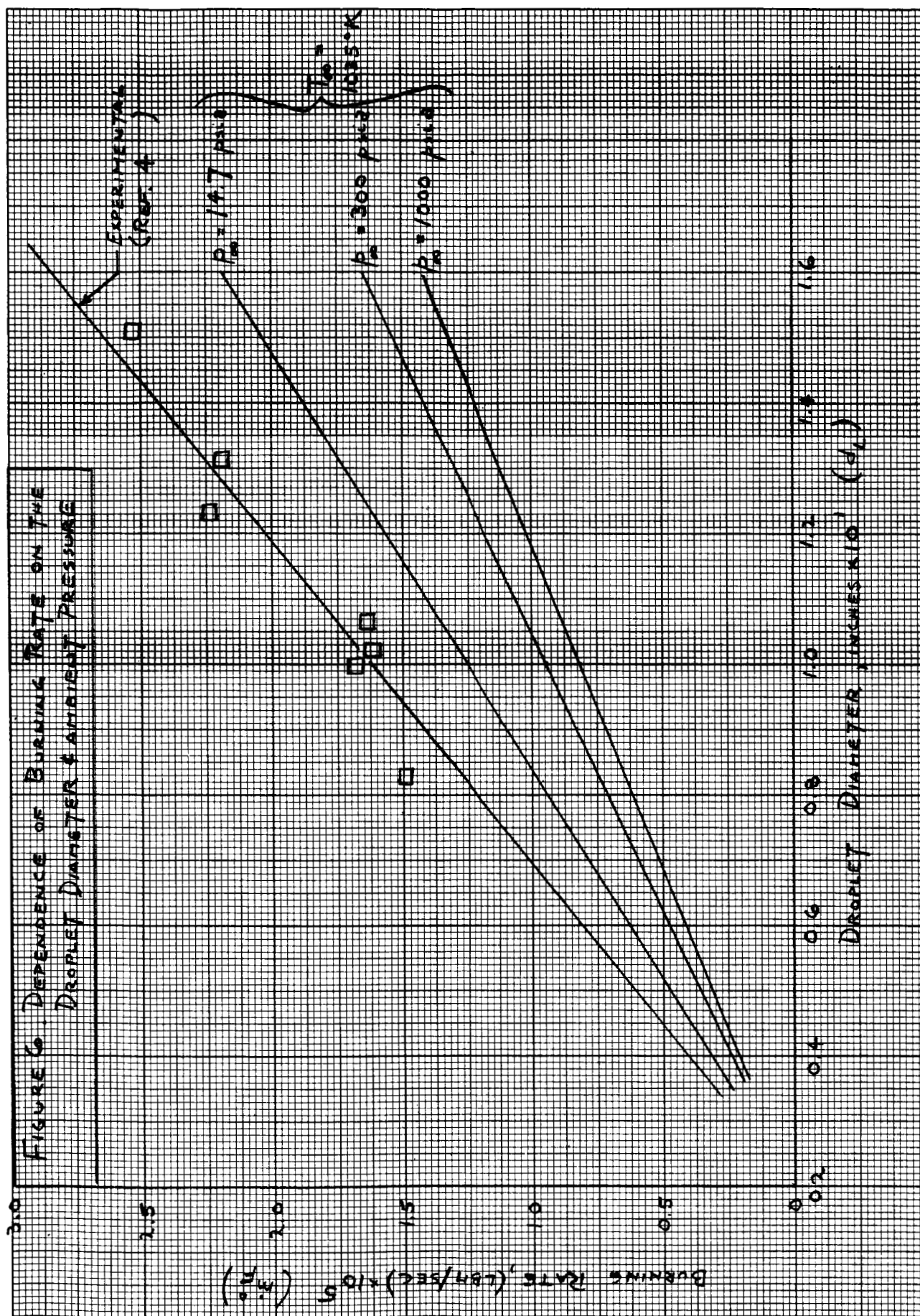
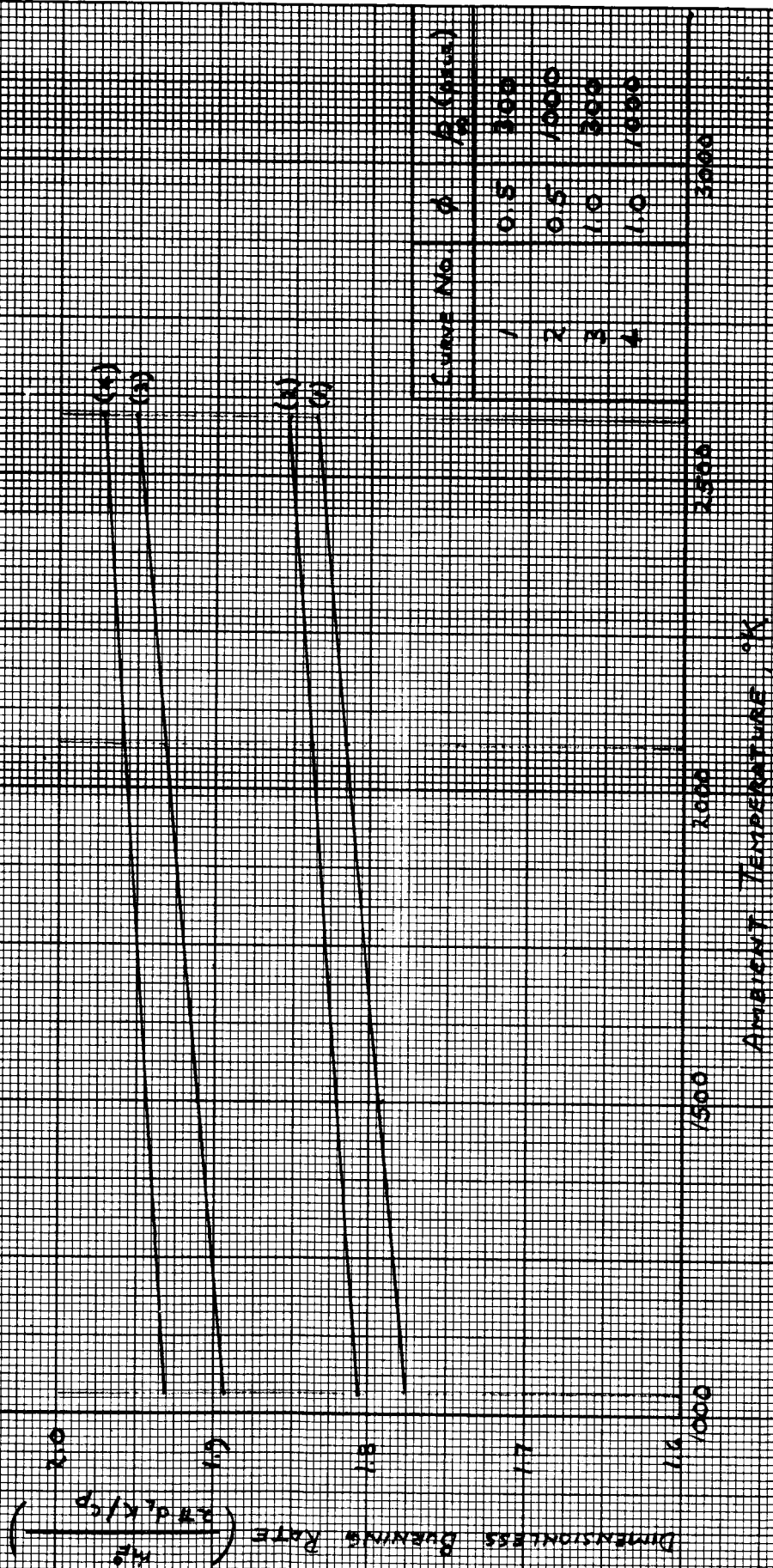


FIGURE 7. THE EFFECTS OF AMBIENT TEMPERATURE & PRESSURE AND EQUIVALENCE RATIO ON THE DIMENSIONLESS BURNING RATE



ratio leads to the expected reduction in W , (b) increasing pressure leads to an increase in W , but a reduction in \dot{m}_F^O (Fig. 6), at least at an ambient temperature of 1035°K (this result will not occur for all values of T_∞), and (c) increasing T_∞ leads to an increase in W .

II. FLUID DYNAMIC MODEL

A. First Row Mesh Point Calculation

In this section we describe a new method of computing the solution to the partial differential equations of a compressible fluid in cylindrical coordinates in the neighborhood of the singular point $r = 0$. In Reference 1, the mesh point at $r = 0$ was computed with the help of contour integrals on the circle of radius Δr (the mesh considered is one in which mesh points are defined by the intersection of curves $r = \text{constant}$ and $\theta = \text{constant}$). All mesh points on $r = \Delta r$ (Δr is the mesh space in the radial direction) cannot be computed by the standard method now being used for interior mesh points because first row points do not have eight nearest neighbors. The following technique is used to define the required eight nearest neighbors.

The method consists in the construction of two temporary sets of data points at $r = \Delta r/2$ and $r = 3\Delta r/2$. These points are obtained by interpolation formulae from information known at $r = 0$, Δr and $2\Delta r$. Higher order formulae would require data at additional points $\dots, -\Delta r, \dots, 3\Delta r, \dots$. A submesh is then constructed in the neighborhood of the ring of radius Δr in which the mesh spacing in the tangential direction is the same as before but the radial mesh size is reduced by a factor of two. The calculation then proceeds as if the set of mesh points with coordinates $(\Delta r, \theta_j, j = 1, \dots, JMAX)$ are interior mesh points. The subroutine which is responsible for this calculation (FRSTRO) has been rewritten

to incorporate the new method. This routine makes use of sub-routine GENPT as a result of the creation of the new mesh points $(\Delta r/2, \phi_j)$ and $(3\Delta r/2, \phi_j)$ on the two respective circles and eliminates some special subroutines that existed in COMB originally.

B. An Exact Solution-Comparison with Machine Experiment

We have considered the exact solution (linearized solution) to the differential equation in the potential ϕ

$$\frac{\partial p}{\partial \rho} \Delta \phi - \phi_{tt} = 0$$

The motion is irrotational so that the velocity in the i^{th} direction u_i is the gradient of the potential ϕ_{x_i} . In addition the requirement that the normal velocity vanish on the boundary S of the chamber

$$\frac{\partial \phi}{\partial n}(x_i, t) = 0, \quad x_i \text{ on } S.$$

We find that

$$\phi = \sqrt{\frac{\partial p / \partial \rho}{K}} \epsilon \quad J_1(Kr) \sin(K \sqrt{\partial p / \partial \rho} t + \theta)$$

and

$$p(r, \phi, t) = p = \gamma p_{\infty} K \epsilon \quad J_1(Kr) \cos(K \sqrt{\partial p / \partial \rho} t + \theta)$$

The velocity components are

$$u = \sqrt{\frac{\partial p}{\partial \rho}} \epsilon \quad J_1'(Kr) \sin(K \sqrt{\frac{\partial p}{\partial \rho}} t + \theta)$$

$$v = \sqrt{\frac{\partial p}{\partial \rho}} \epsilon (Kr)^{-1} J_1(Kr) \cos(K \sqrt{\frac{\partial p}{\partial \rho}} t + \theta)$$

Figures (8) and (9) give the density field ($p^{1/\gamma}$) and the pressure field at the start of the computation, $p = p(r, \phi, 0)$. This is a graphical representation of the linearized solution. The above velocity components go into the construction of the velocity field which is shown in Figure (12); however, this plot corresponds to the finite amplitude case which will be discussed later. The

velocity plots scale, the maximum and minimum value for the infinitesimal case is 10^{-5} those values shown in Figure (12). Figure (10) shows the pressure field after 600 cycles of calculation; the non-dimensional time at this point is 5.69 (x.131 millisec - .746 millisec real time) and the wave has undergone 1.62 revolutions or approximately 2,200 rev/sec (period = 460 μ -sec). Figure (11) shows the corresponding field obtained from the exact solution - the results are virtually identical; if the two plots are superimposed, the point of maximum pressure is congruent.

The solution will, if calculations are allowed to continue, appear to undergo uniform rotation at the given period. No distortions or asymmetries appear. Nonlinear effects, the bunching of the isobars in the compression portion of the field, are absent. This characteristic property is absent in the next problem considered.

C. A Finite Amplitude Calculation of a Rotating Wave

Only one parameter has been changed in the previous calculation; that parameter is the maximum pressure (450 psia). The velocity field at $t = 0$ corresponding to this pressure is given in Figure (12). Figures (12)-(18) show in detail, the motion of the velocity field up to 600 cycles of computation (corresponding to a value of non-dimensional time of $1.857 \times 2.18 = 4.05$; all time values for the finite amplitude case should be multiplied by this factor 2.18, i.e., Figures (12)-(36)). From Figures (18) to (21) a plot of the velocity field each 600 cycles of computation is shown. It is clear that

- a) the velocity field does not remain symmetric;
- b) an induced flow is generated behind the
compression wave;
- c) this flow is fully developed in about one
period of rotation.

Figure (21) was plotted poorly due to the Calcomp having a stuck pen; the actual velocity is not as large as indicated at the chamber walls.

Figures (22) to (31) are the contours of the density field corresponding to the previous figures which represented the velocity field. Figure (22) is the initial field at $t = 0$. It is clear, by scanning through these figures that one observes that

- a) the density field steepens in the leading edge
of the compression pulse and spreads in the
region of the trailing edge;

- b) this steepening is most pronounced in the first half to three quarters of the first period;
- c) a periodic ($\omega t + 2\pi$) continuous wave solution seems to be the asymptotic solution ($t \rightarrow \infty$). A total of about $4 \frac{3}{4}$ rotations were computed and shown in these figures.

These observed effects are clearly nonlinear in nature.

Figures (32) to (36) are the plots of the pressure field at intervals of 600 cycles. The initial pressure distribution is shown in Figure (32). The pressure pulse steepens up to a maximum in about one period and then is approximately constant ~ 1.6 (575 psia).

D. Convergence of the Difference Equations

It is to be expected that as the mesh gets finer and finer, the solution will converge to the differential equation. The truncation error for the approximation used in this calculation is second order every where (except for the evaluation of the interpolated data for the first row calculation). As the space step decreases the dissipation of the scheme should decrease, i.e., finer meshes should lead to sharper results. We have tried two meshes, the finer one (all the results presented have been computed on this mesh), 10 points in r and 36 points in θ , and the coarse one, 5 points in r and 18 points in θ . The figures (37), (38) and (39) give the value of the density, pressure and velocity at a non-dimensional time of 14.7 for the coarse mesh. These results may be compared to the fine mesh solution at 2400 cycles which, in turn, corresponds to a non-dimensional time of 16.0. It is clear that much of the detail of the solution is absent in the formal calculation. The two tables which follow give some additional means for comparing the two solutions.

5 x 18 MESH

Cycle	t/to	p _{max}	\vec{U}_{max}	p _{min}	ρ_{max}	ρ_{min}
600	14.7	1.244	0.414	0.521	1.37	0.665
540	13.3	1.35	0.393	0.559	1.47	0.709
480	11.8	1.49	0.379	0.586	1.49	0.744
420	10.4	1.45	0.369	0.571	1.58	0.721
360	8.9	1.42	0.397	0.502	1.46	0.651
300	7.4	1.21	0.378	0.505	1.44	0.654
240	5.9	1.44	0.376	0.517	1.49	0.669
180	4.4	1.57	0.342	0.581	1.59	0.740
120	3.0	1.55	0.409	0.557	1.62	0.716
60	1.6	1.35	0.393	0.533	1.45	0.691
0	0.0	1.25	0.358	0.417	1.40	0.561

10 x 36 MESH

Cycle	t/to	p _{max}	\vec{u}_{\max}	p _{min}	ρ_{\max}	ρ_{\min}
2400	16.0	1.67	0.434	0.547	1.74	0.704
1800	12.5	1.59	0.440	0.542	1.67	0.701
1200	7.8	1.51	0.385	0.509	1.61	0.666
600	4.05	1.83	0.448	0.562	1.87	0.715
540	3.66	--	0.454	---	1.94	0.729
420	2.92	--	0.486	---	1.70	0.720
300	2.14	--	0.399	---	1.73	0.655
180	1.31	--	0.472	---	1.50	0.669
60	0.45	--	0.395	---	1.49	0.645
0	0.0	1.25	0.358	0.417	1.40	0.561

E. Simple Forcing Function

Since the non-reacting code is yielding fairly accurate solutions a first attempt at calculating the flow resulting from the differential equation

$$W_t + F_r + G_\phi + S + H_z = \psi, \quad \psi = \begin{pmatrix} 0 \\ 0 \\ 0 \\ \dot{E} \end{pmatrix}$$

where the forcing function ψ , which has a single component \dot{E} is given by

$$\dot{E} = \text{const} |(p-1)|^v, \quad v = \frac{1}{2} \text{ if } (p-1) < 0 \\ v = 1 \text{ if } (p-1) \geq 0$$

subject to the initial data and boundary conditions of the problem described in Section C.

At $t = 0$, the energy is switched on. Since the energy release is biased towards high pressures the most intense region of combustion occurs about $\theta=0$ near the boundary (where $r=R$). A very strong wave, turning into a shock, is propagating in towards the chamber center almost symmetric about $\theta=0$. Figures (40) and (41) show the pressure field and velocity field after $10.5 \mu\text{sec}$ ($= .0376 \times 2.18 \times .131 \cdot 10^{-3}$). The pressure reaches approximately 20,600 psia, while the maximum value of the velocity is approximately 10,000 ft./sec. (2.87×3500). The harshness of these results indicate the intensity of the energy source. This calculation became unstable at the center after approximately 30 cycles. The shock has not yet reached this point. This calculation is to be

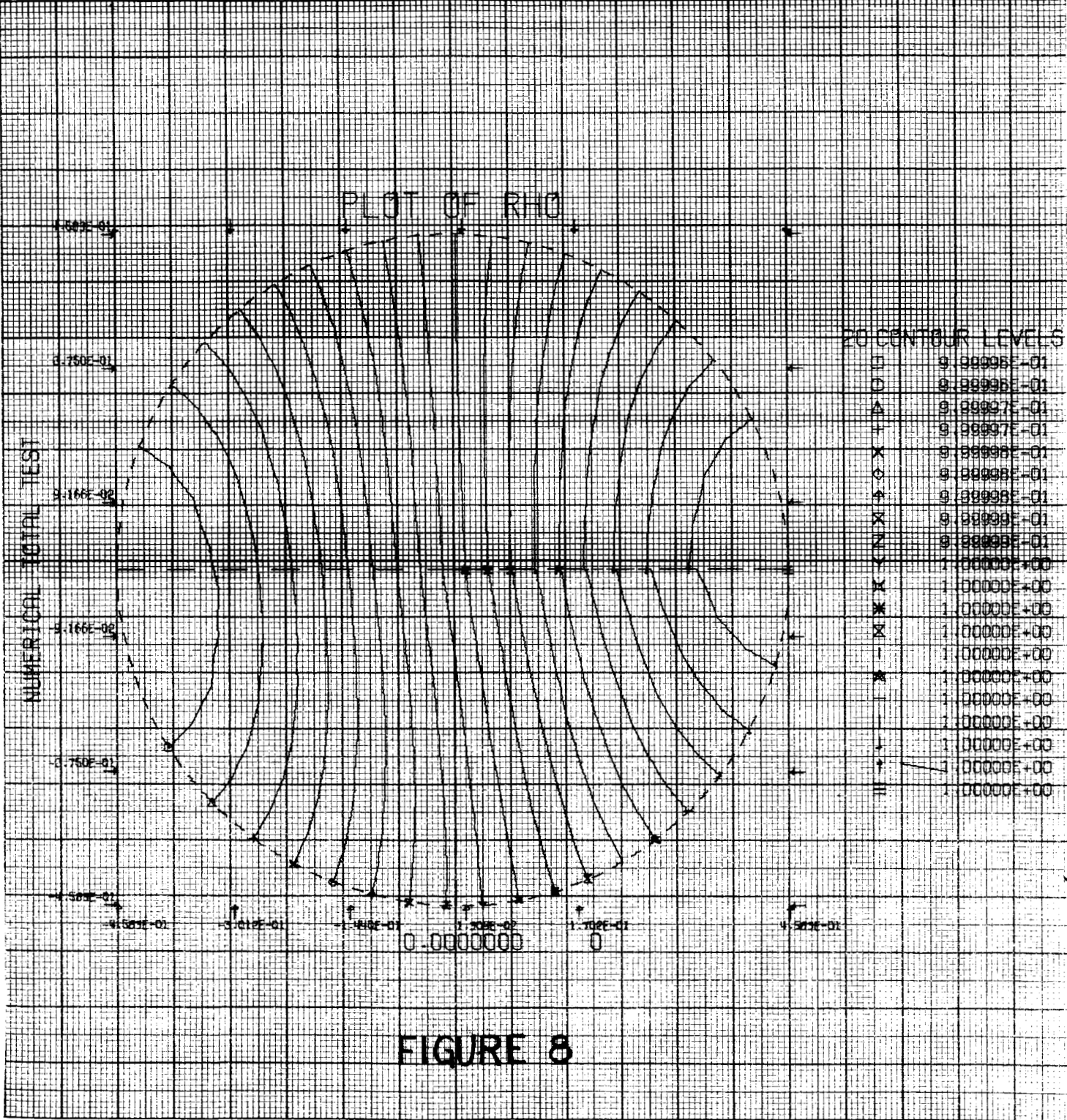
considered only as an exploratory effort and it is interesting only in that the severe gradients generated behave well, i.e., the difference equations seem stable in the region which contains a strong shock.

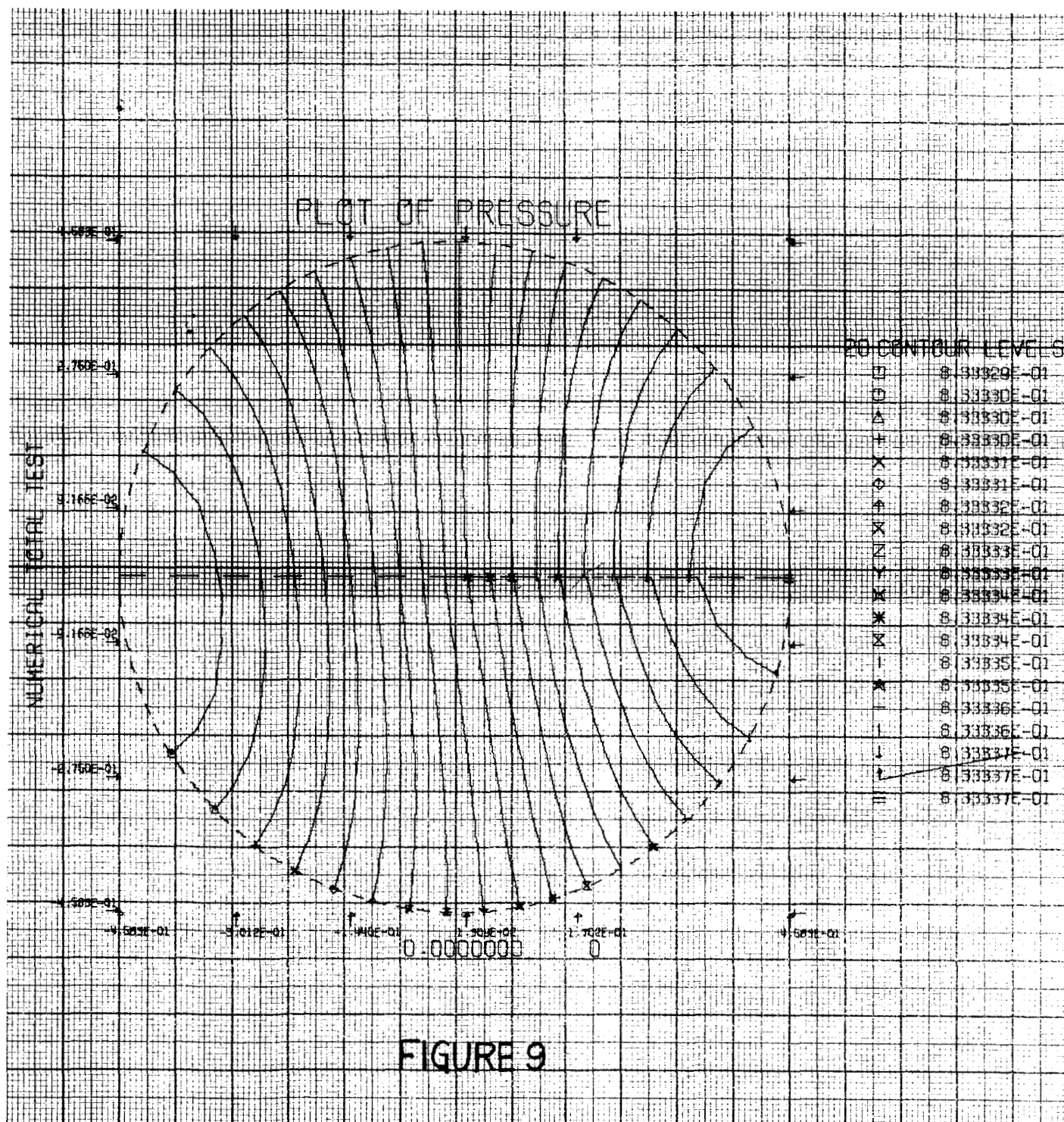
F. Program COMB Status

The forcing function is being changed in program COMB. There are two modifications in progress. One concerns using the simple function described in Section E. Rather than switching on the energy source immediately, we plan to allow the calculation to run several tens of cycles (to allow equilibrium of the data on the discrete mesh to occur) and then turn on this source, not at once but rather slowly. Perhaps it may require a full rotation of the finite amplitude wave around the chamber before the energy is completely turned on.

The second change will allow the coupling of the actual chemical and droplet (which has been discussed in the first two sections of the report) model to the gas dynamic model.

In addition, a still finer mesh (on which the numerical solution is obtained) is to be used to compare the convergence of the solution with the two calculations reported in Section D. This mesh will contain 72x20 mesh points.





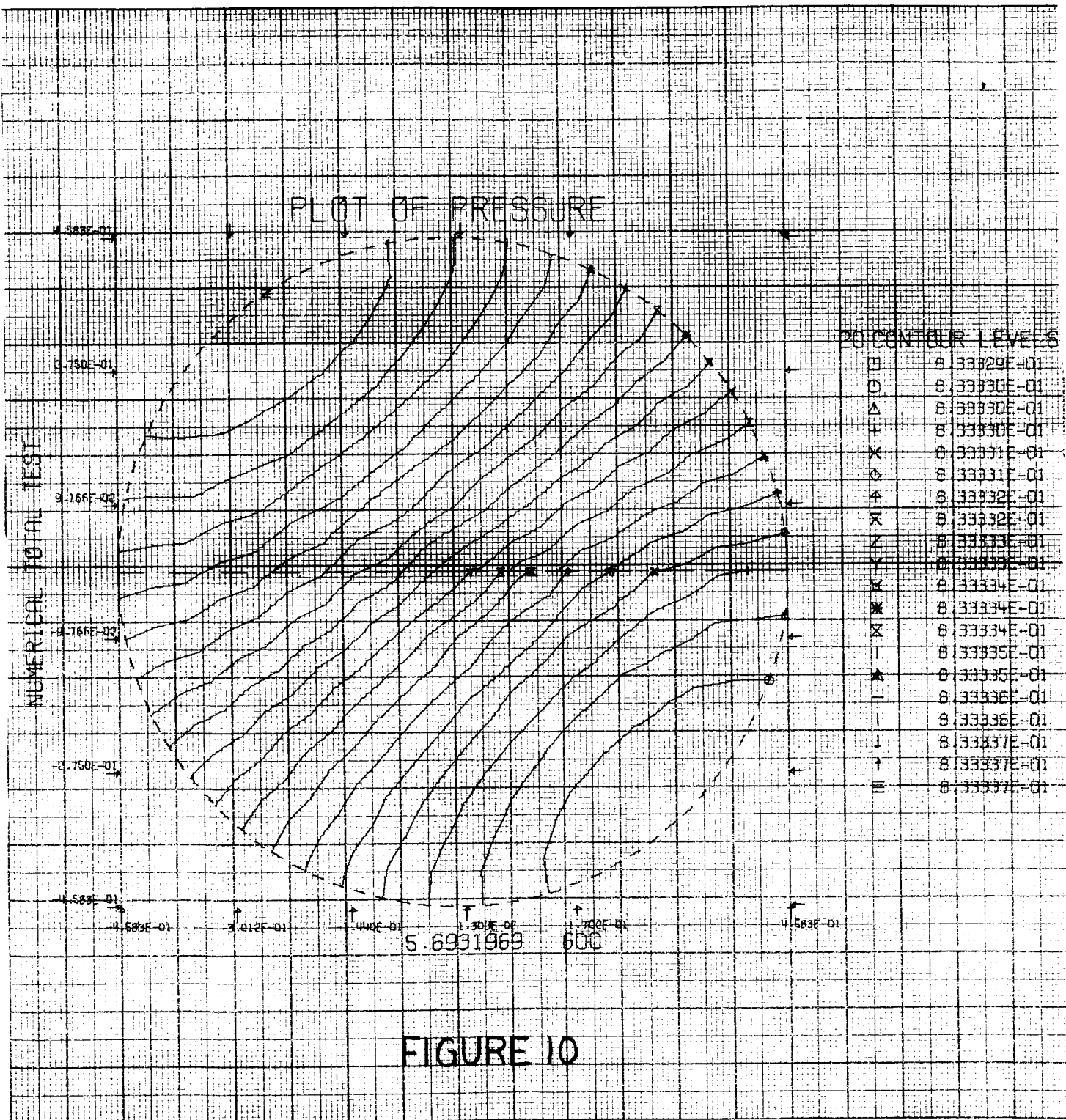
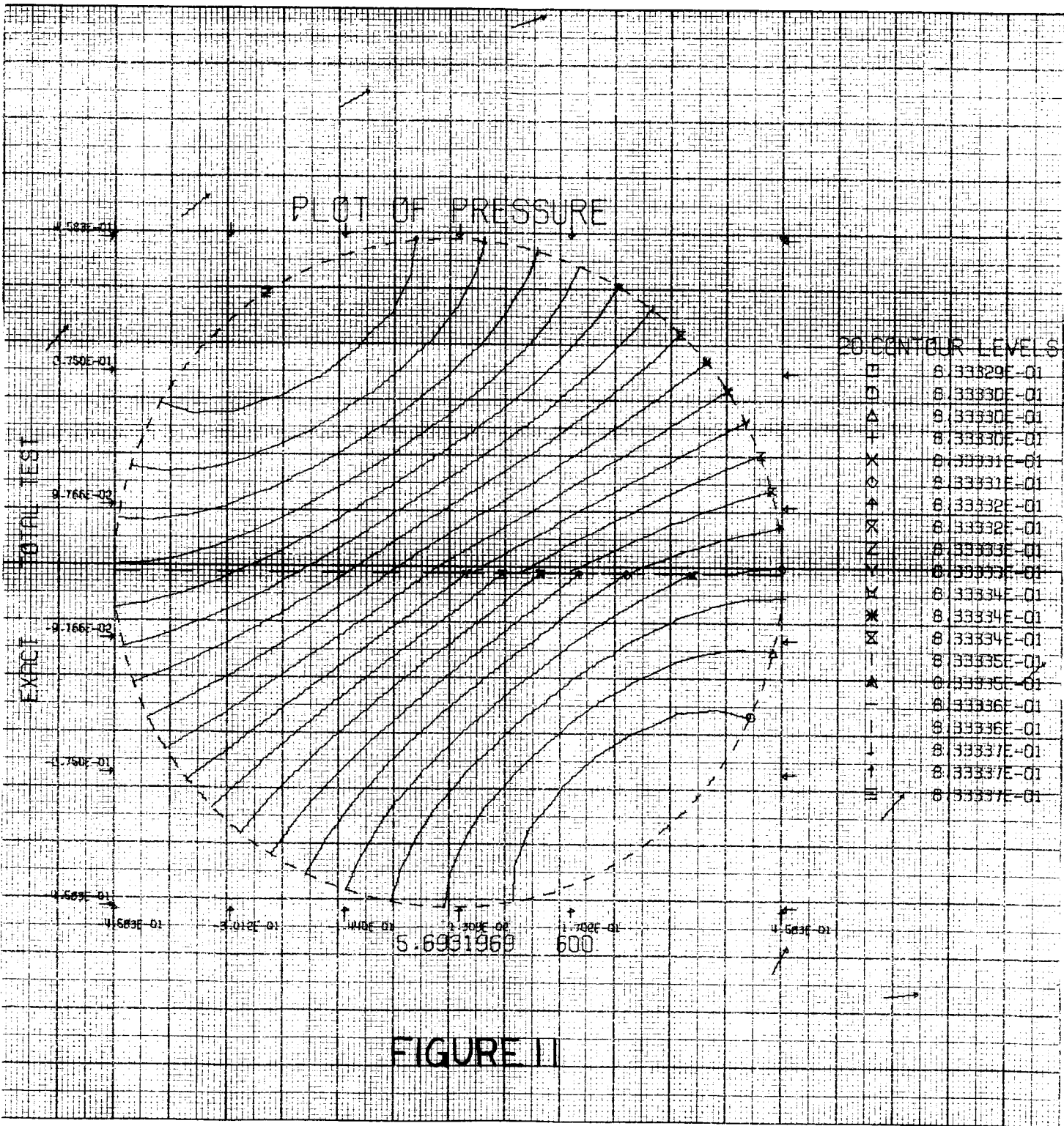


FIGURE 10



VECTOR PLOT OF UMAG

VECTOR .50 INCHES LONG = $3.58E-01$. VALUES $\leq 4.30E-02$ ARE .06 INCHES LONG.

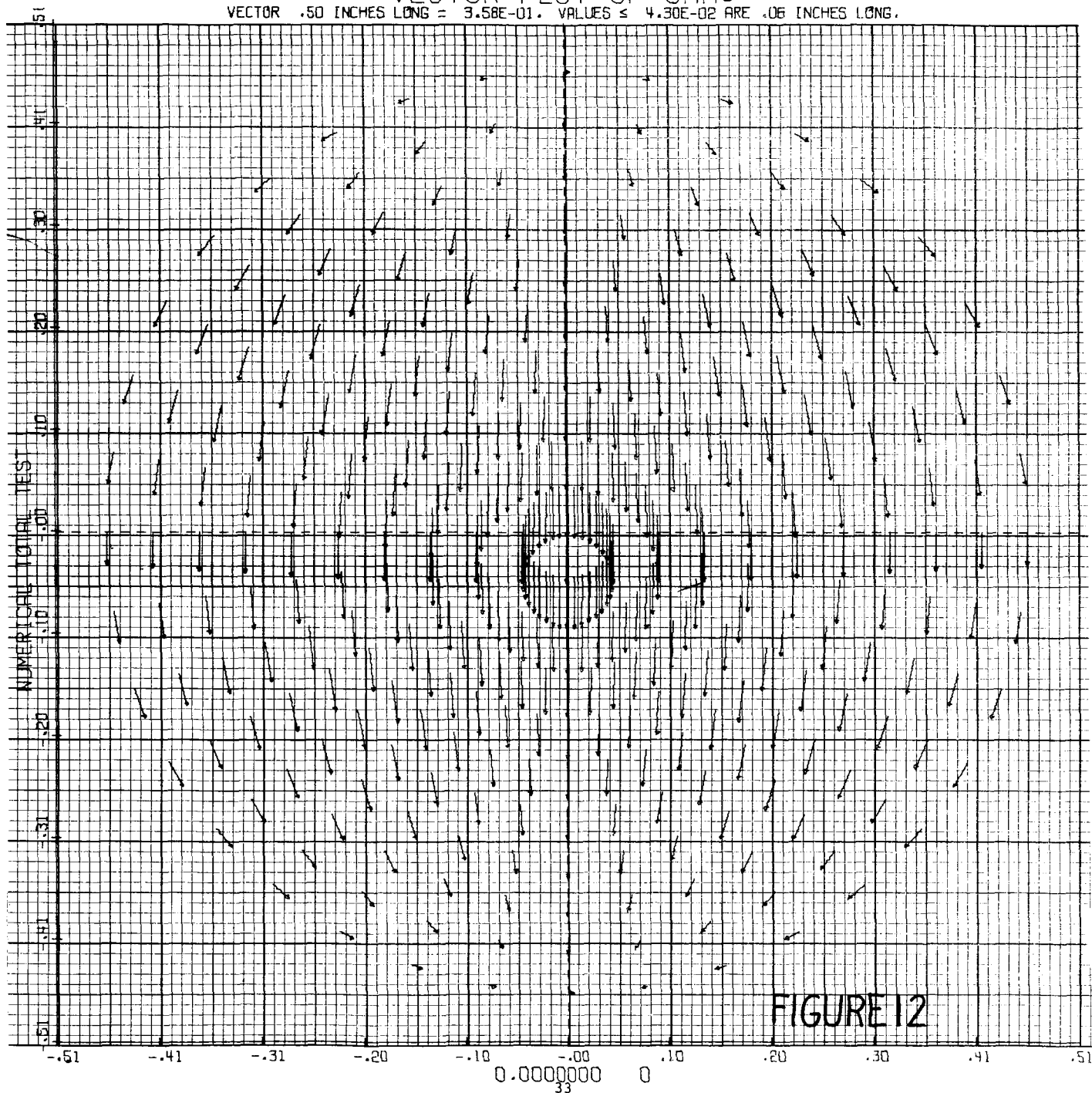
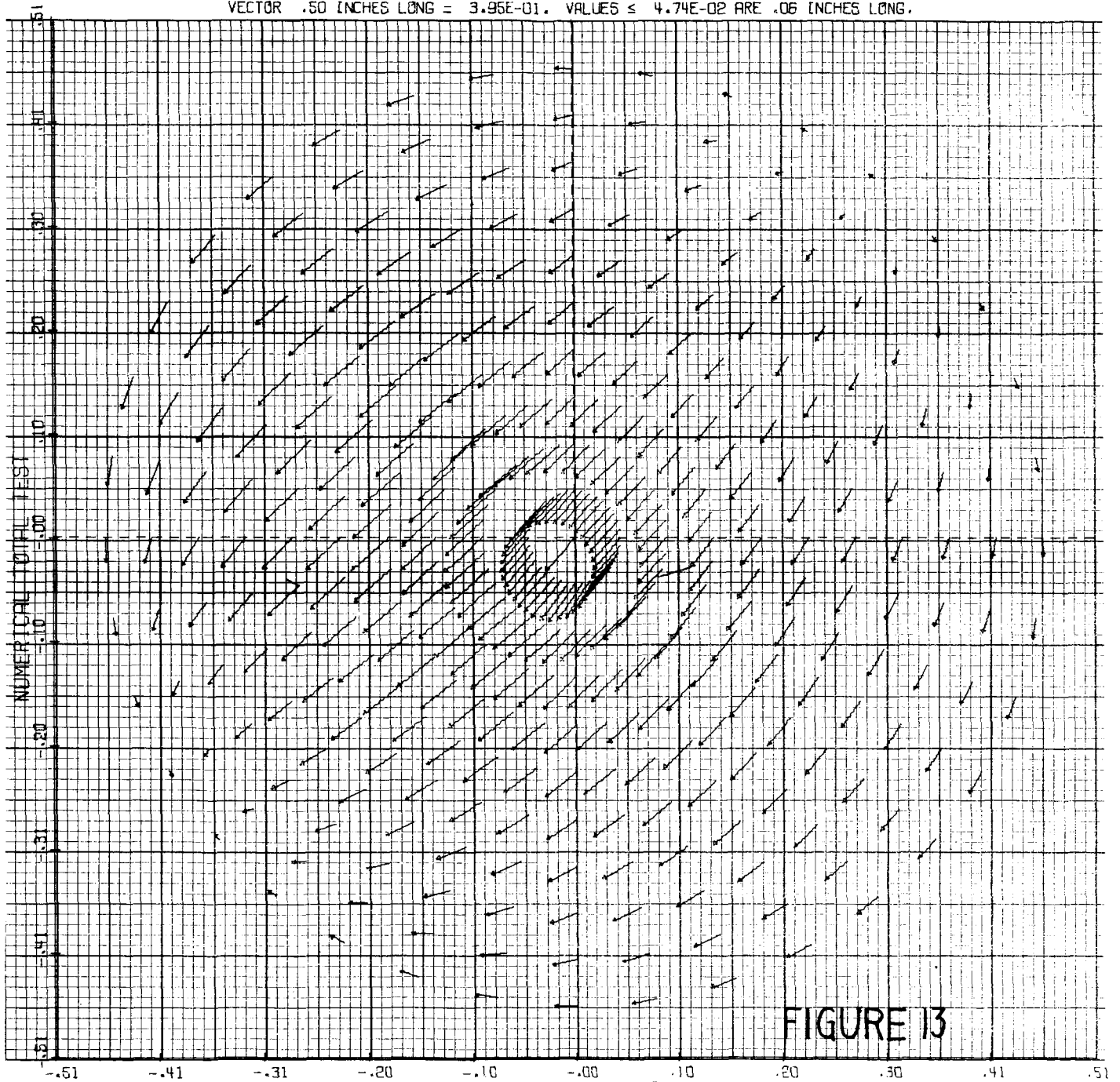


FIGURE 12

VECTOR PLOT OF UMAG

VECTOR .50 INCHES LONG = $3.95E-01$. VALUES $\leq 4.74E-02$ ARE .06 INCHES LONG.



.2037970 60
34

VECTOR PLOT OF UMAG

VECTOR .50 INCHES LONG = $4.72\text{E}-01$. VALUES $\leq 5.67\text{E}-02$ ARE .06 INCHES LONG.

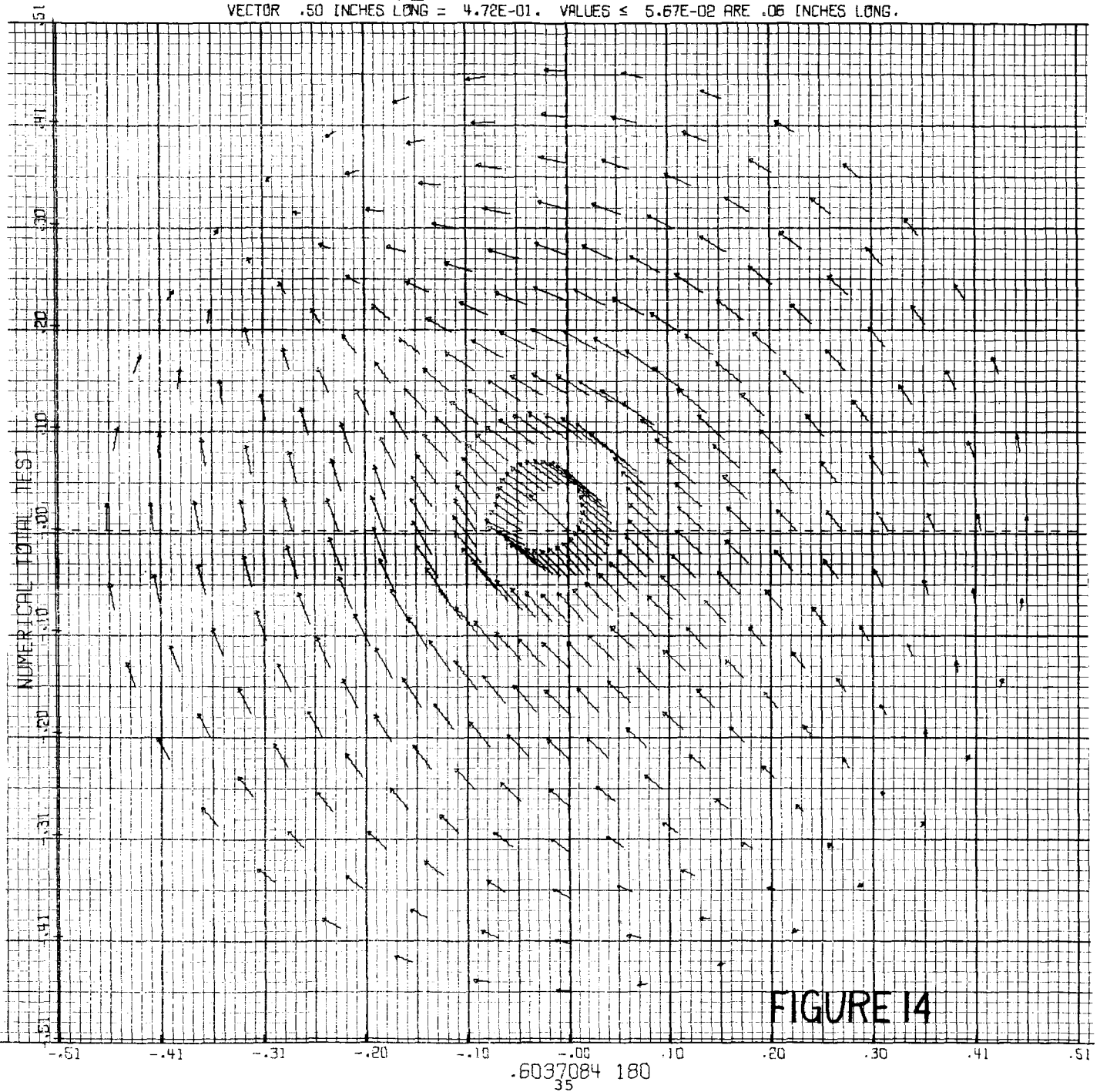
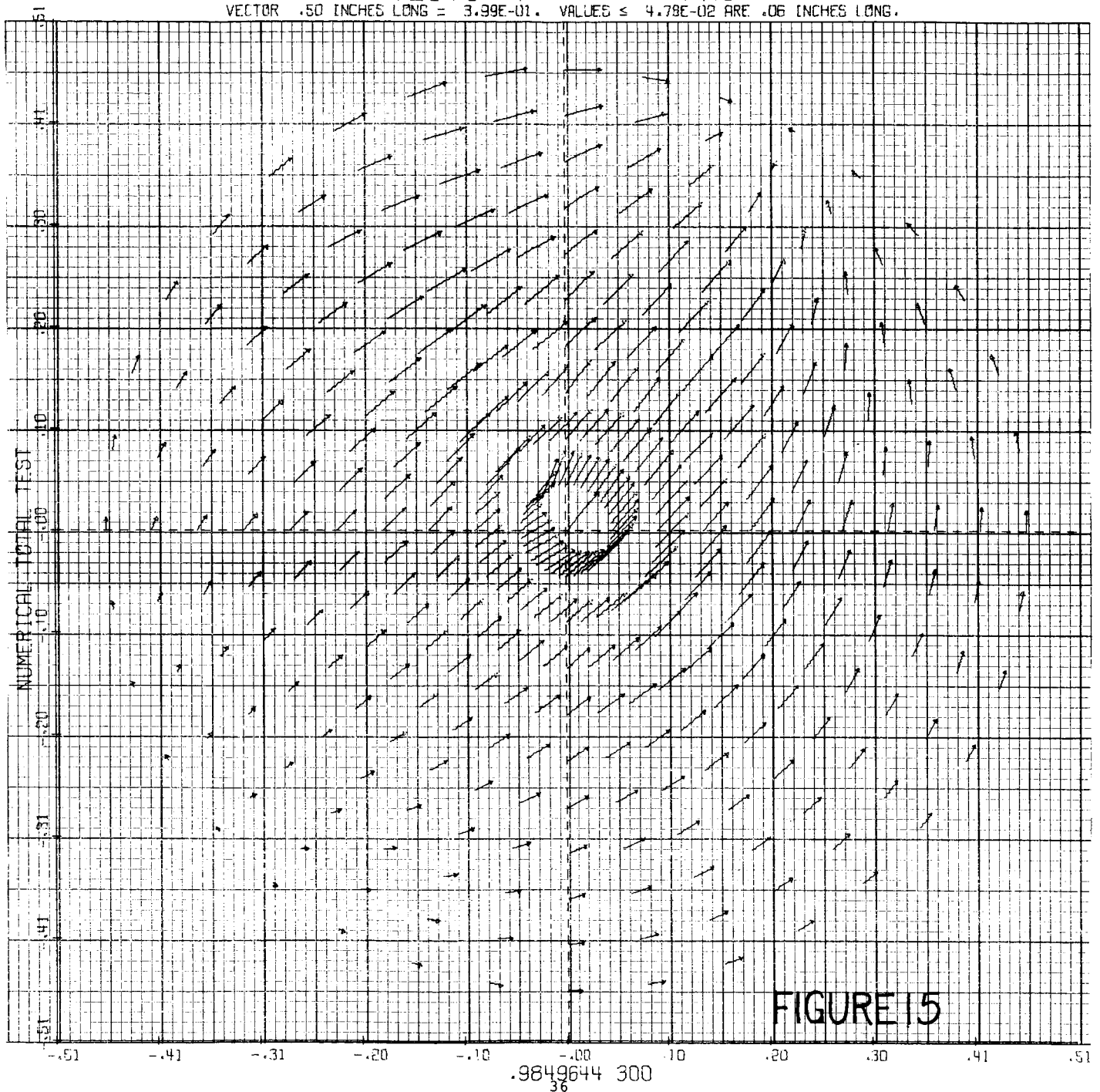


FIGURE 14

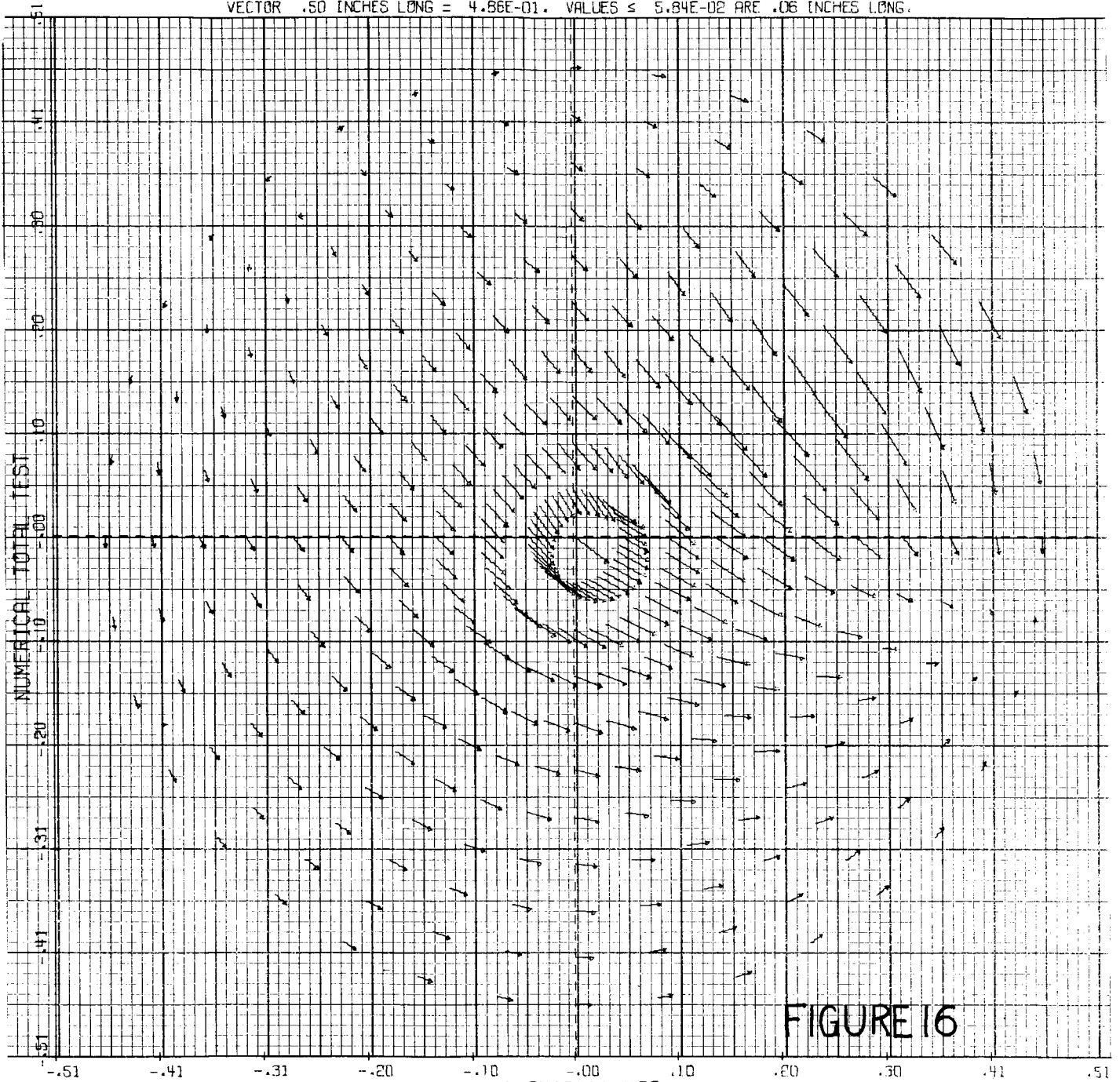
VECTOR PLOT OF U_{MAG}

VECTOR .50 INCHES LONG = $3.99E-01$. VALUES $\leq 4.78E-02$ ARE .06 INCHES LONG.



VECTOR PLOT OF UMAG

VECTOR .50 INCHES LONG = $4.86E-01$. VALUES $\leq 5.84E-02$ ARE .06 INCHES LONG.



1.3410111 420
37

VECTOR PLOT OF U_{MAG}

VECTOR .50 INCHES LONG = $4.54E-01$. VALUES $\leq 5.45E-02$ ARE .06 INCHES LONG.

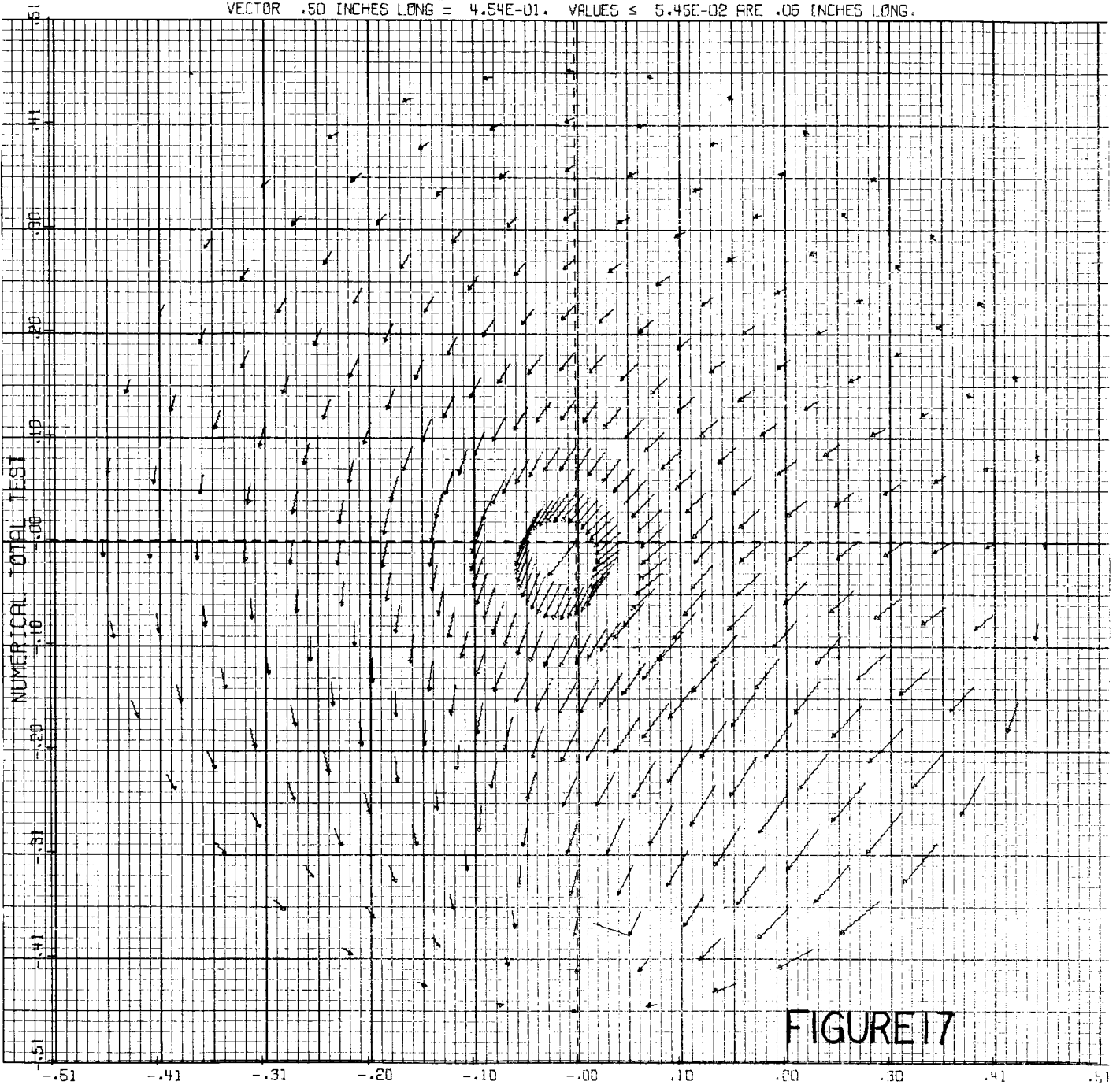


FIGURE 17

1.6876577 540
38

VECTOR PLOT OF U_{MAG}

VECTOR .50 INCHES LONG = $4.48E-01$. VALUES $\leq 5.37E-02$ ARE .06 INCHES LONG.

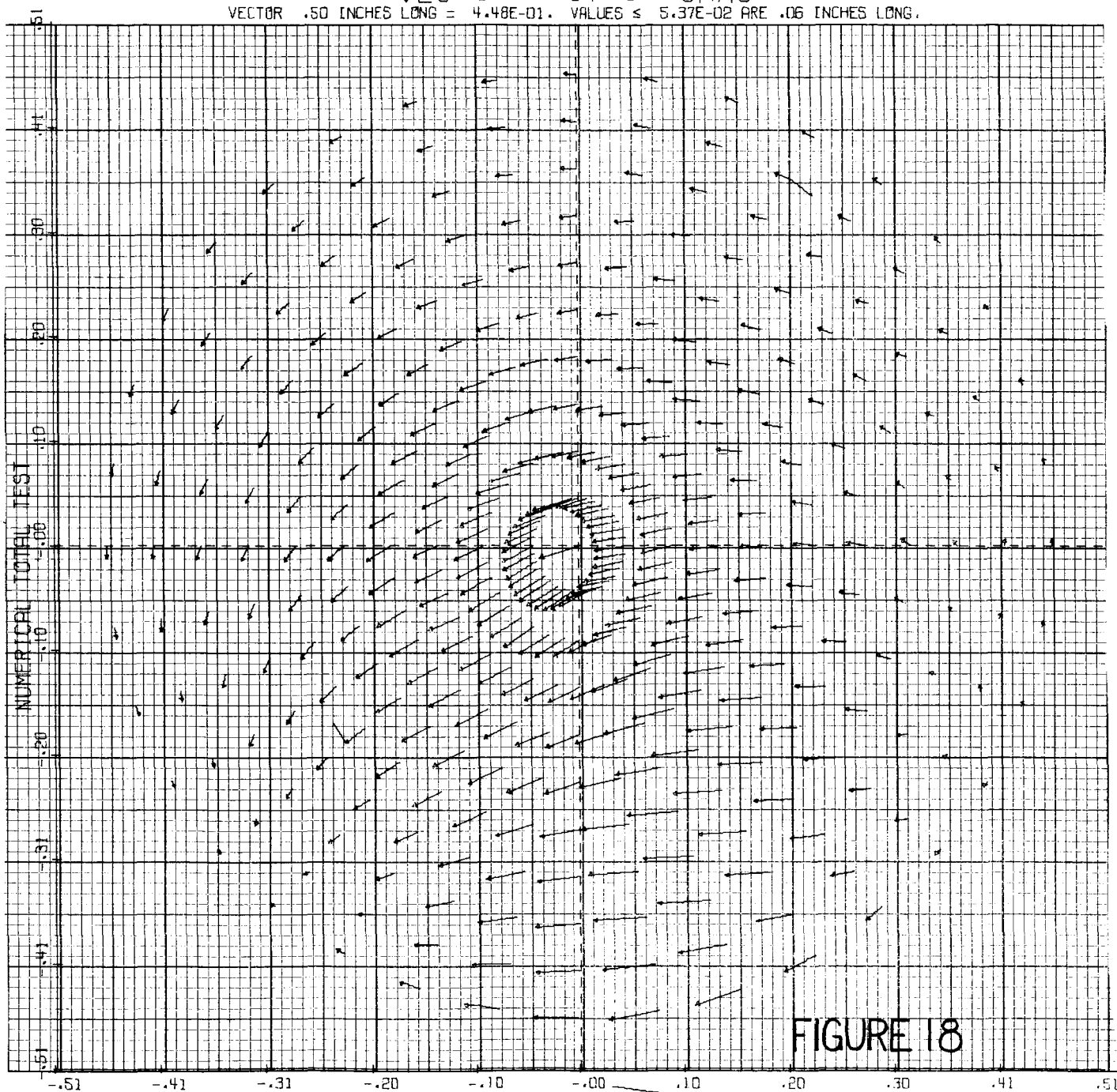


FIGURE 18

8572334 600
39

VECTOR PLOT OF UNAG

VECTOR .50 INCHES LONG = $3.85E-01$. VALUES $\leq 4.62E-02$ ARE .06 INCHES LONG.

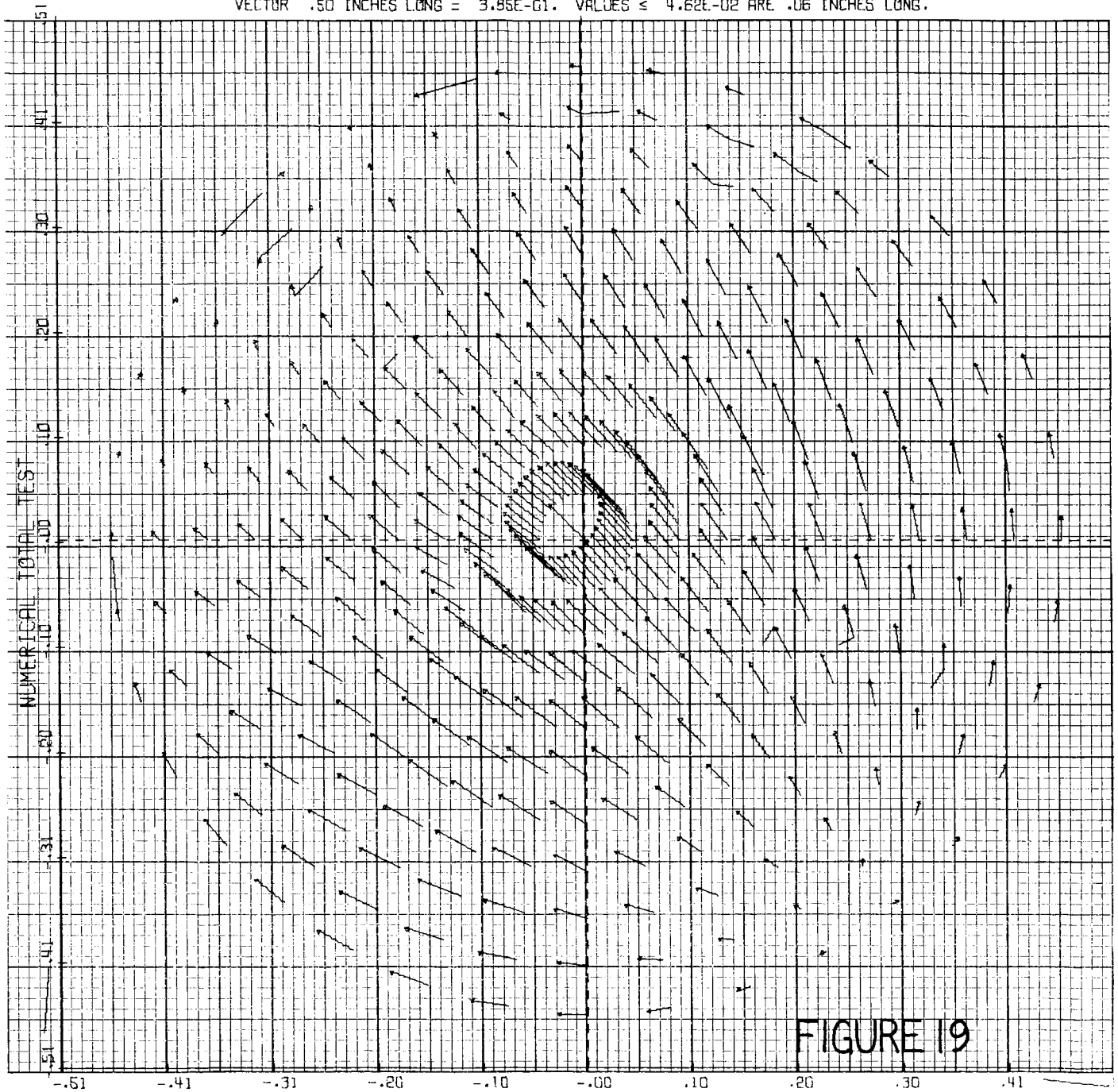
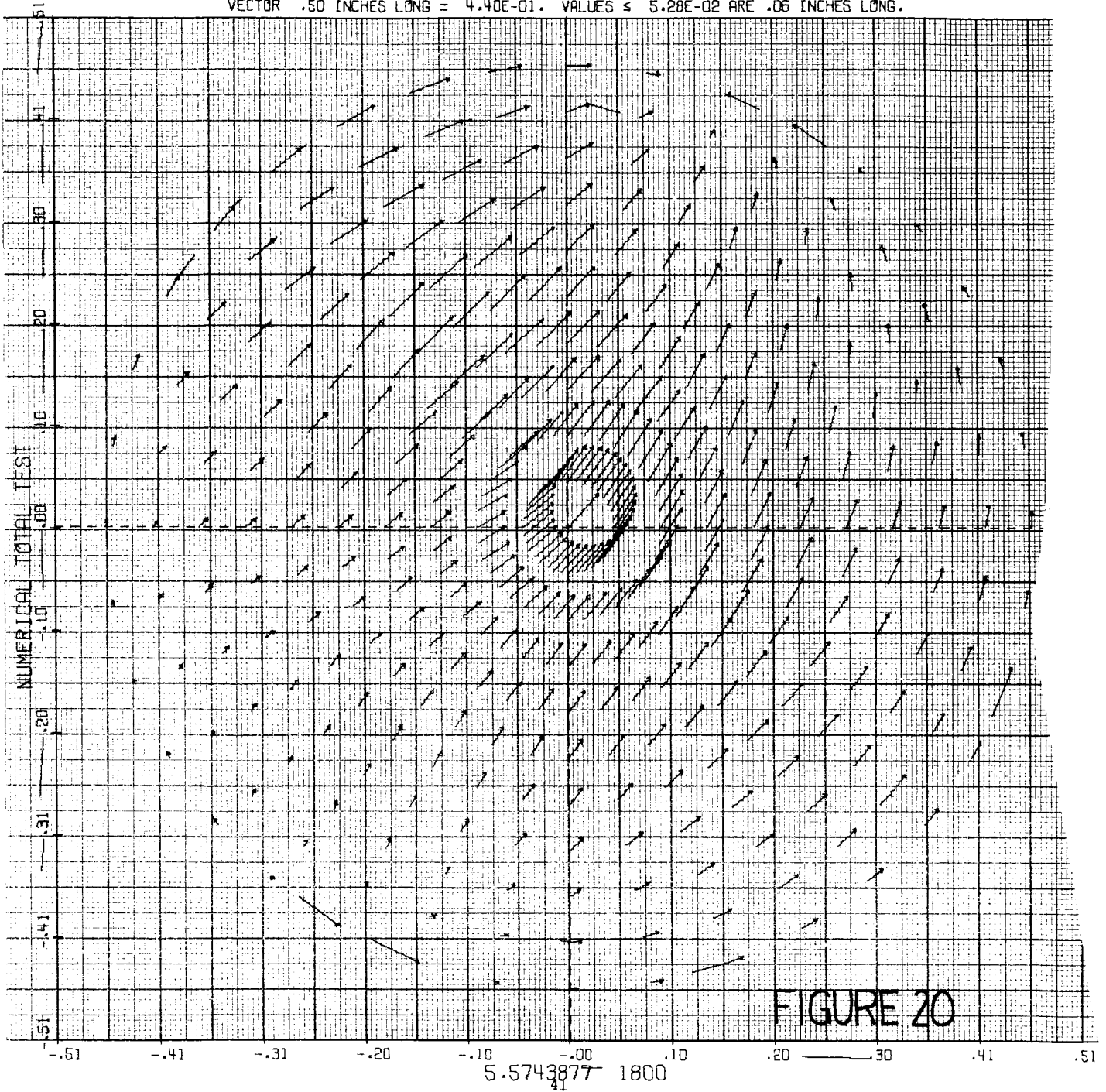


FIGURE 19

3.64172691200
40

VECTOR PLOT OF UMAG

VECTOR .50 INCHES LONG = $4.40E-01$. VALUES $\leq 5.28E-02$ ARE .06 INCHES LONG.



VECTOR PLOT OF UMPG

VECTOR .50 INCHES LONG = $4.34E-01$. VALUES $\leq 5.21E-02$ ARE .06 INCHES LONG.

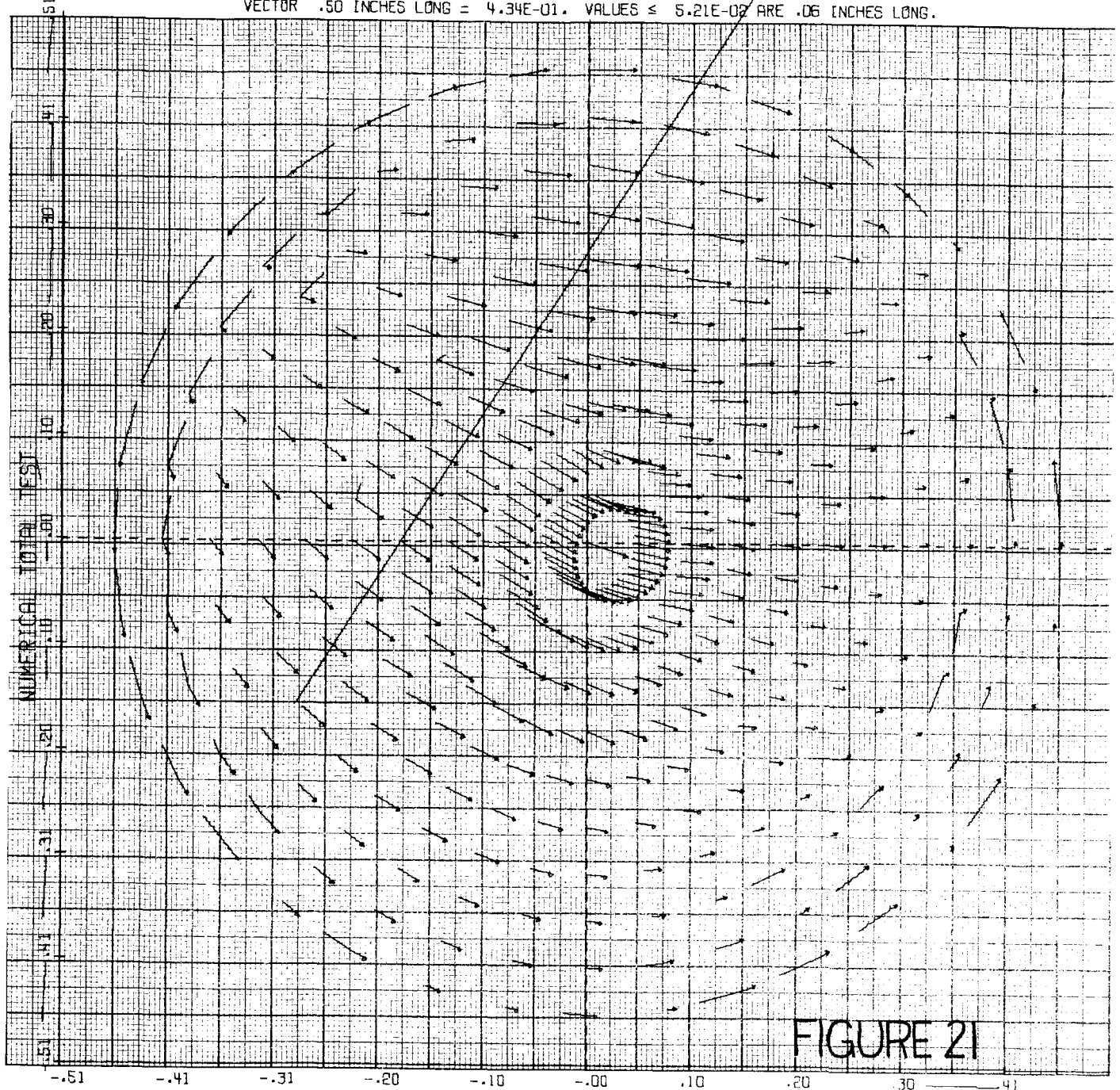
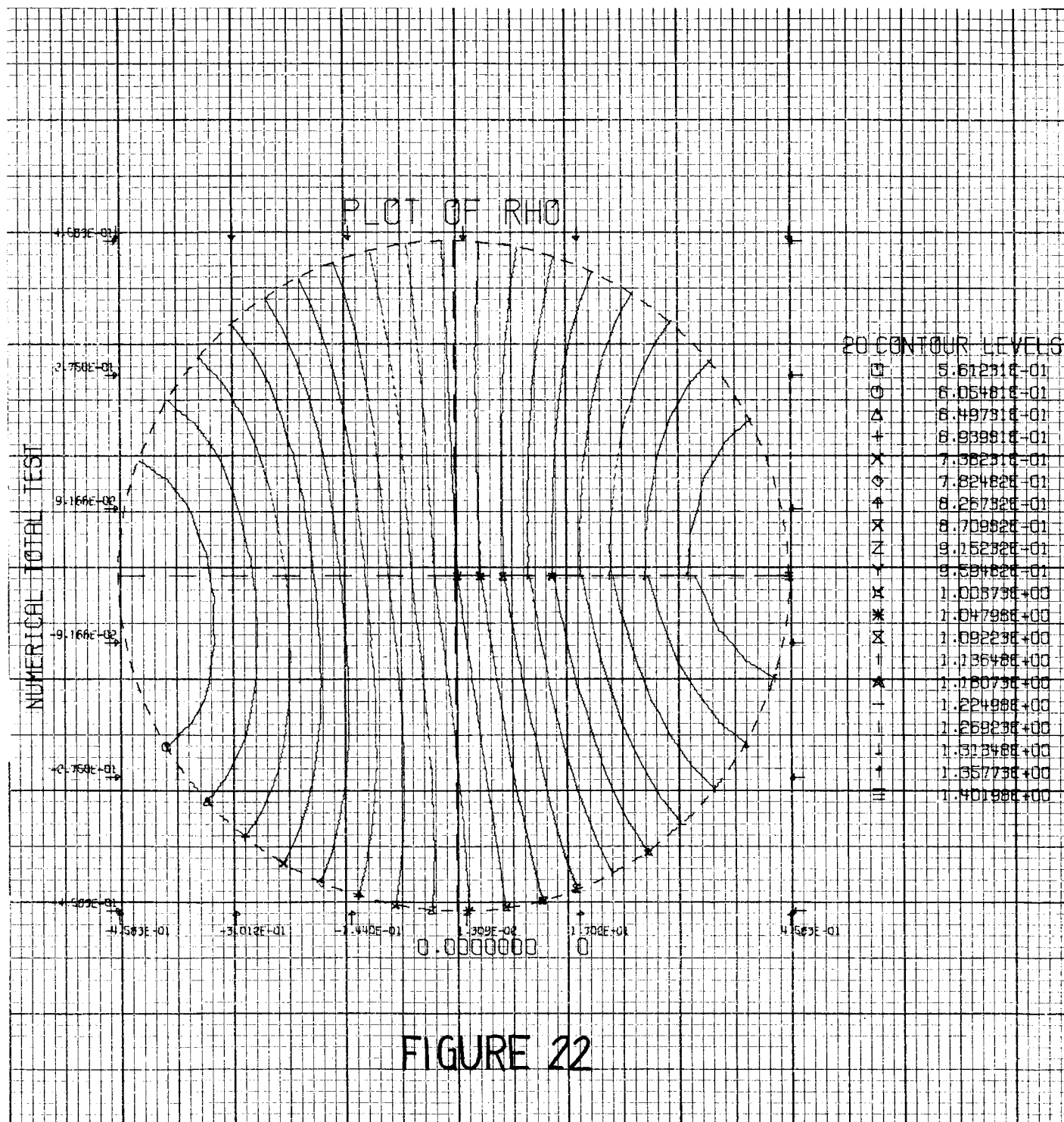
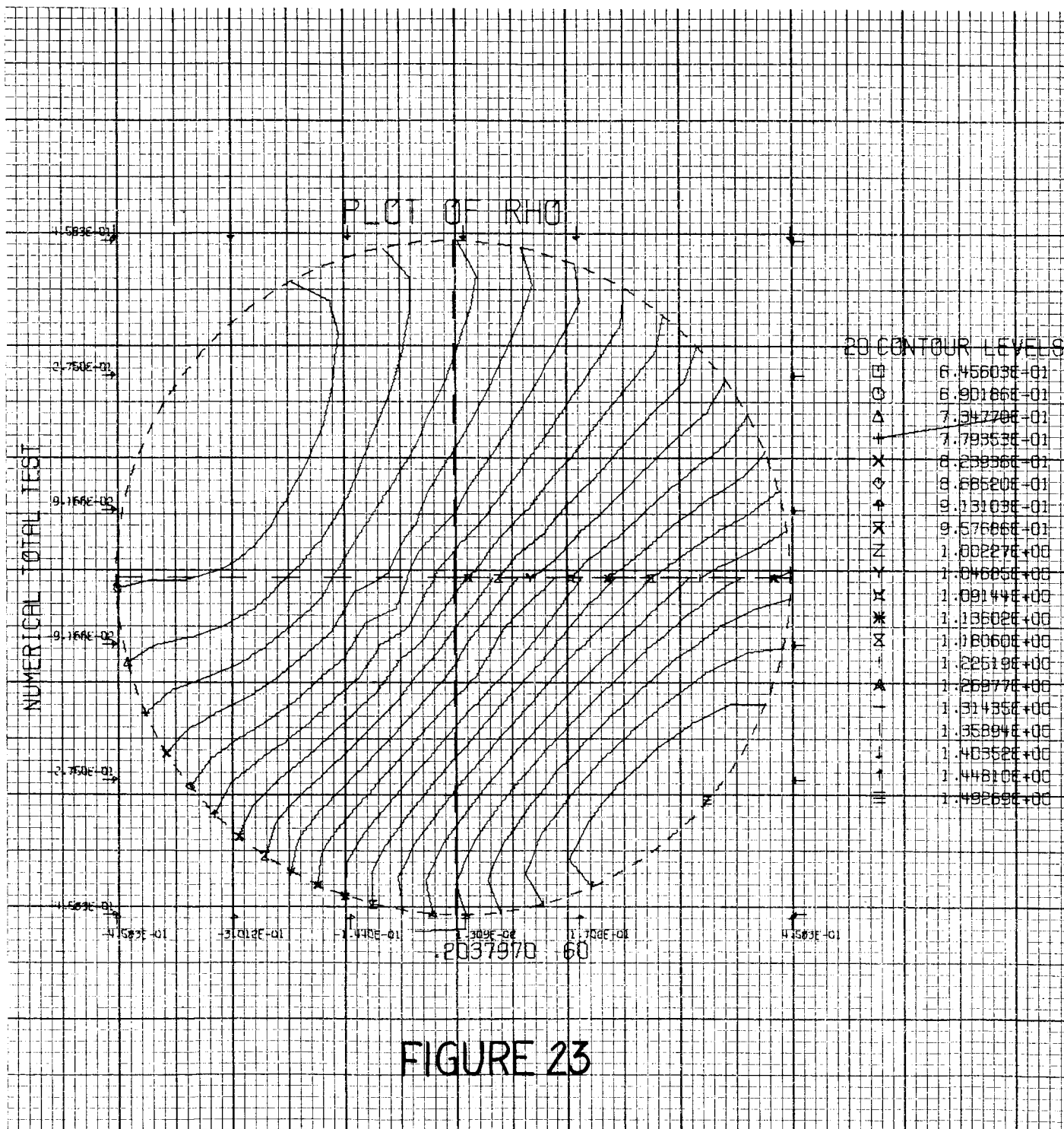


FIGURE 21

7.3539052 2400
42





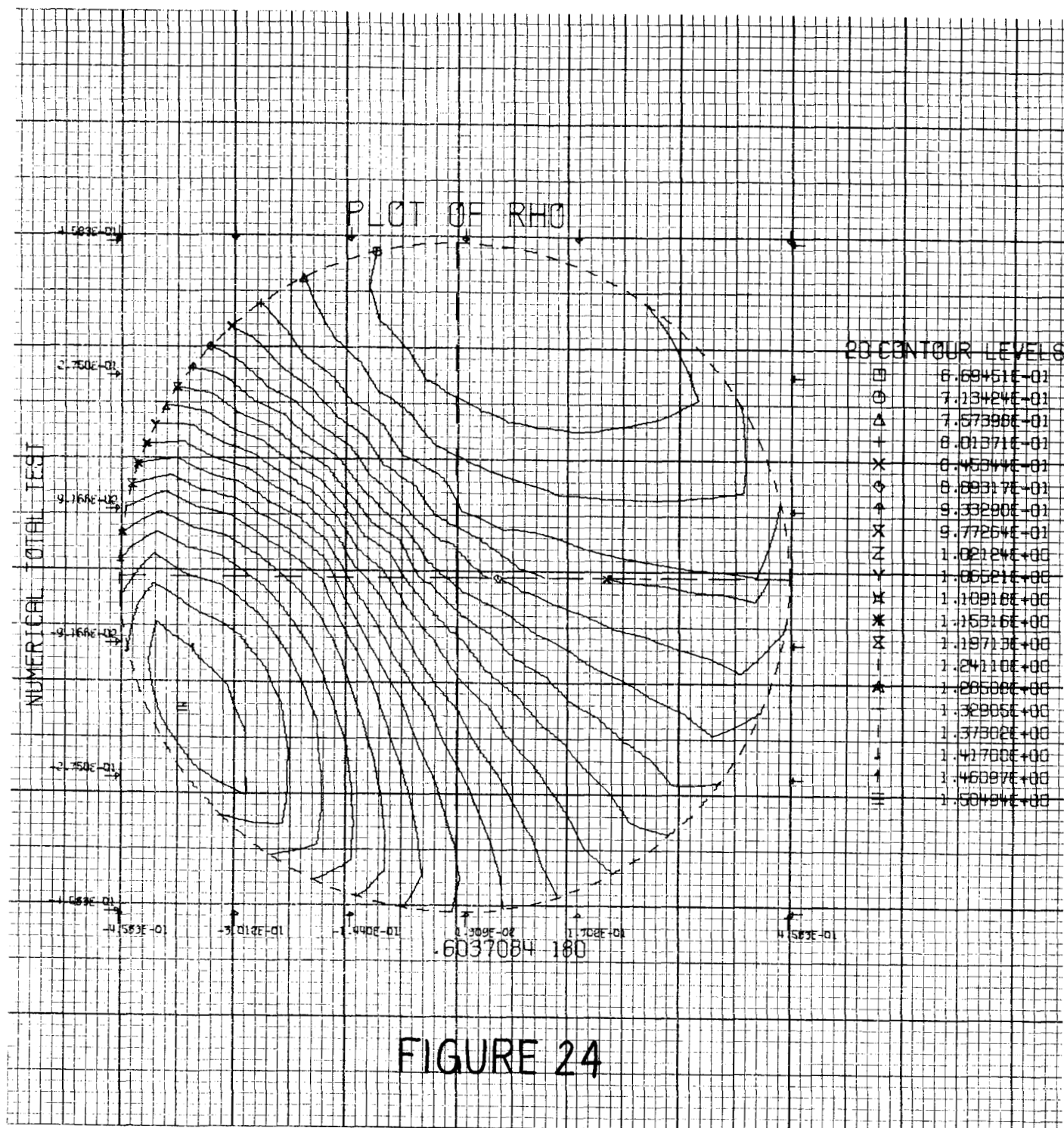
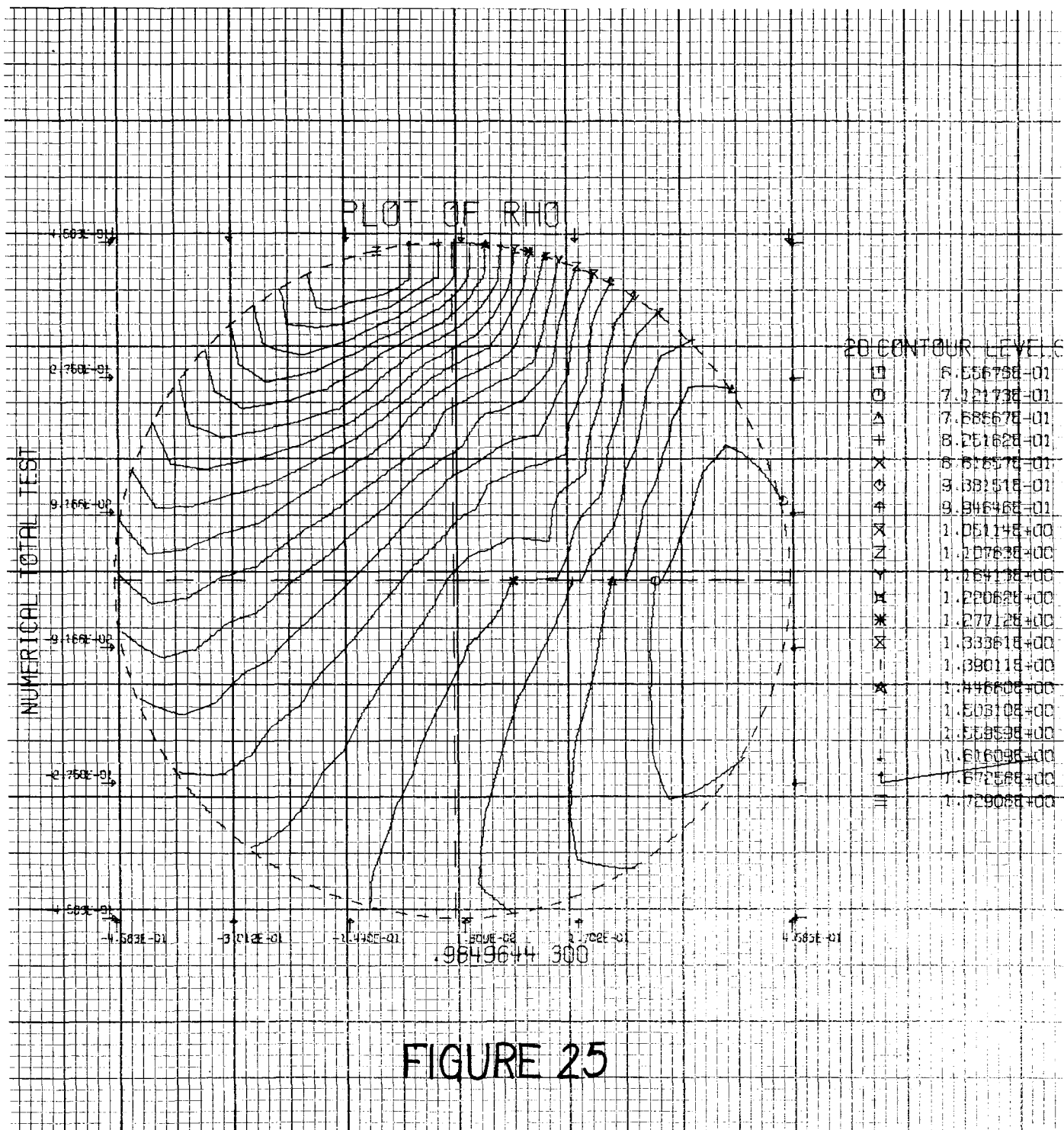
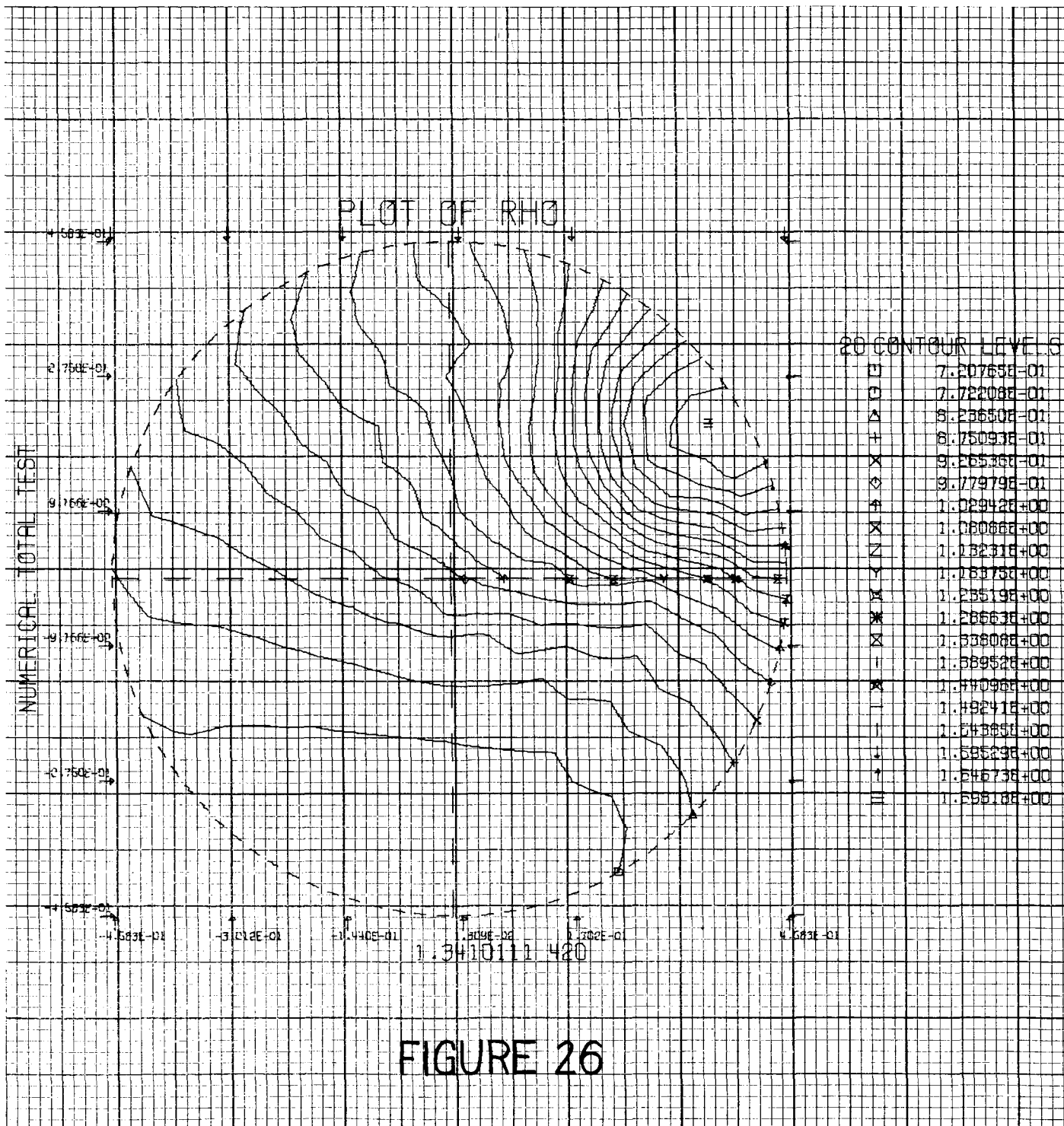


FIGURE 24





PLOT OF RHO

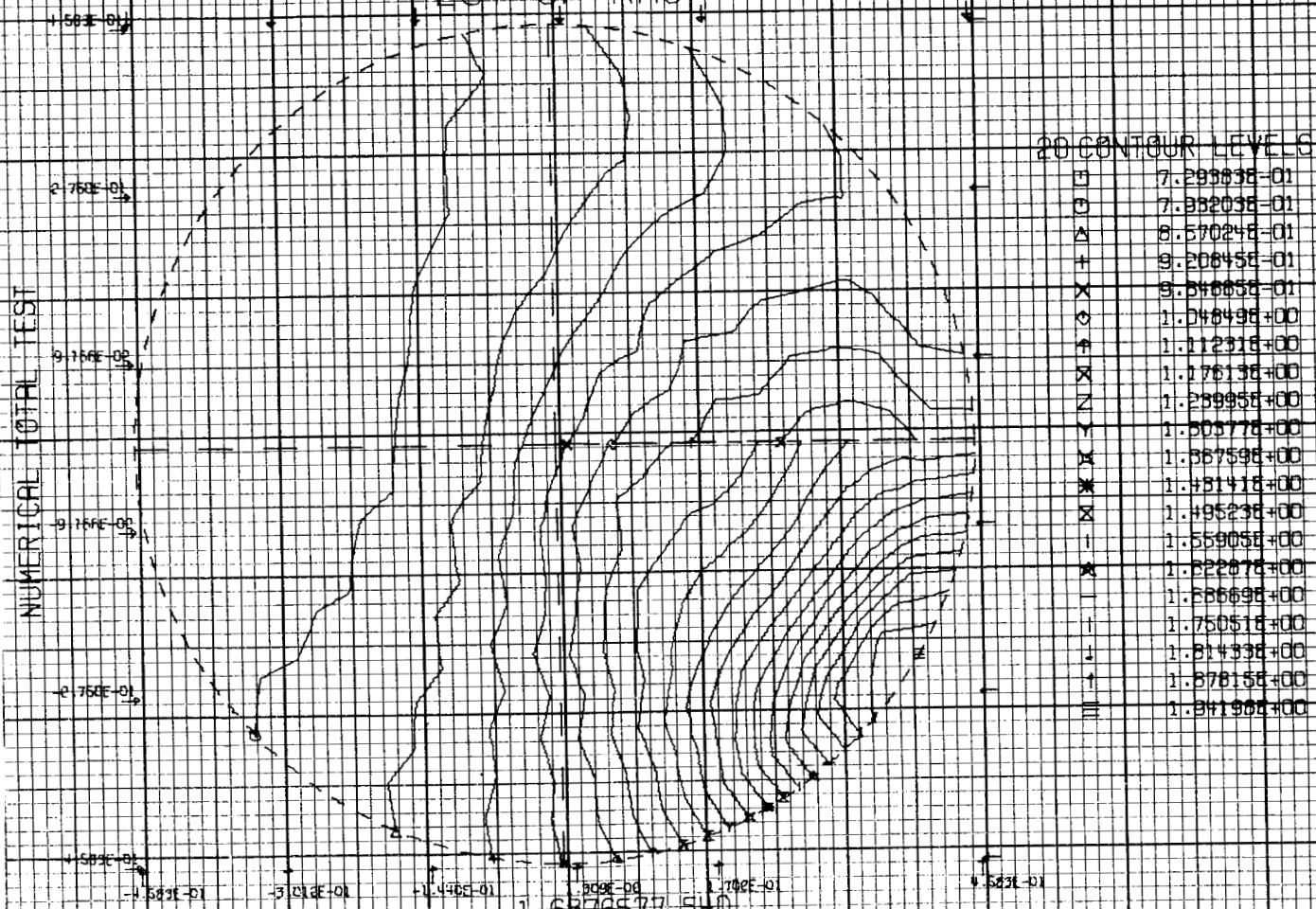
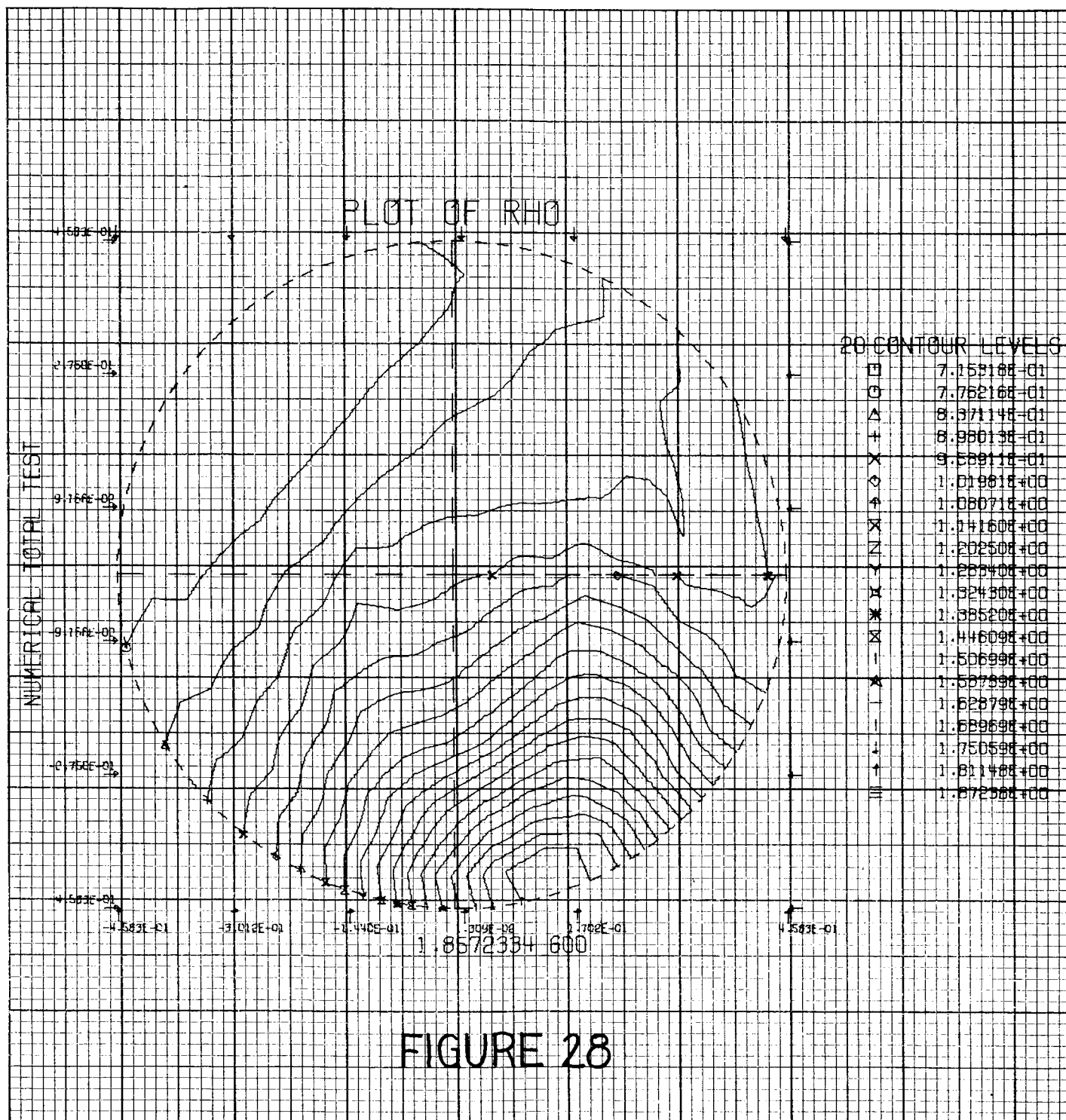
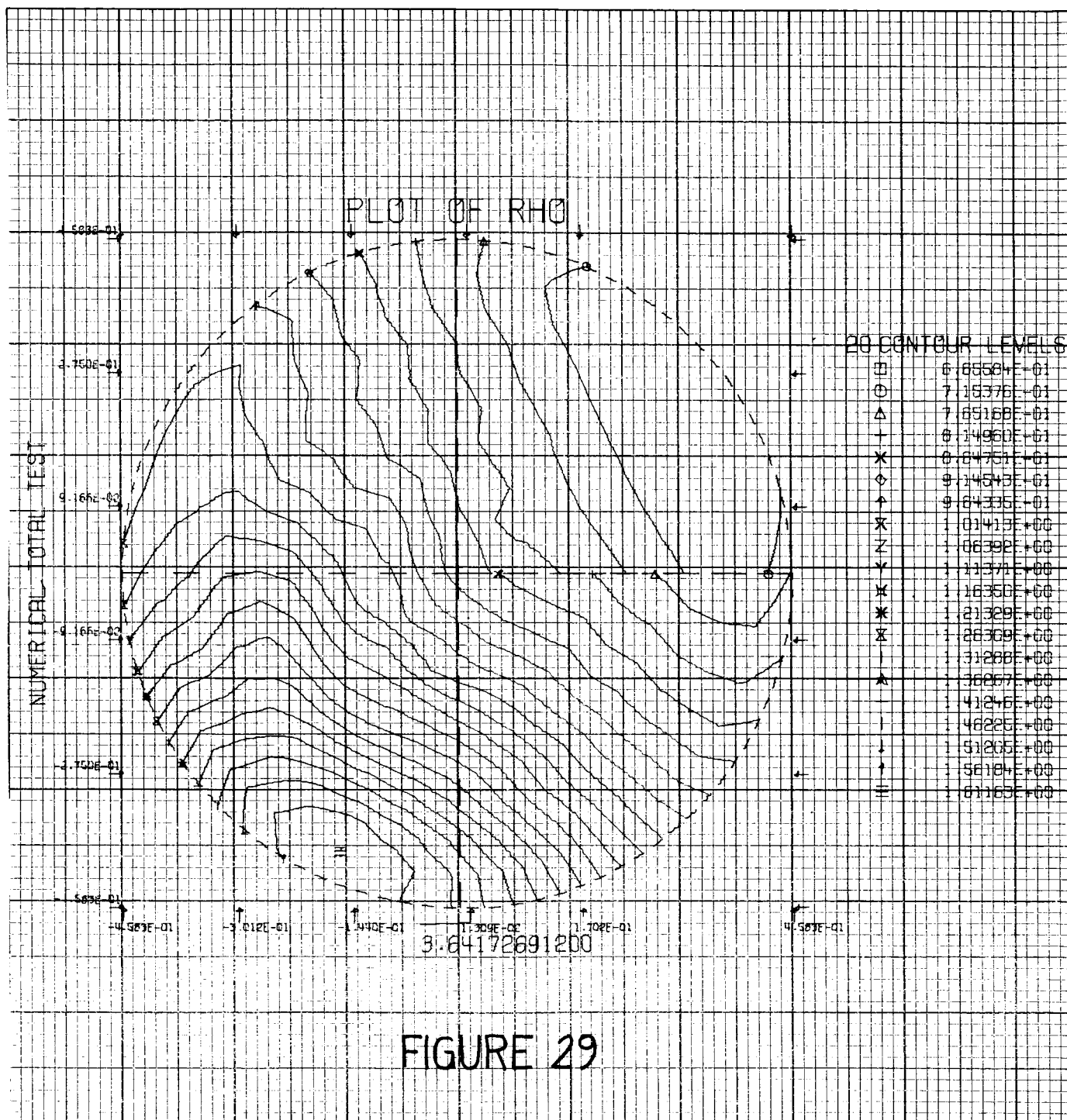
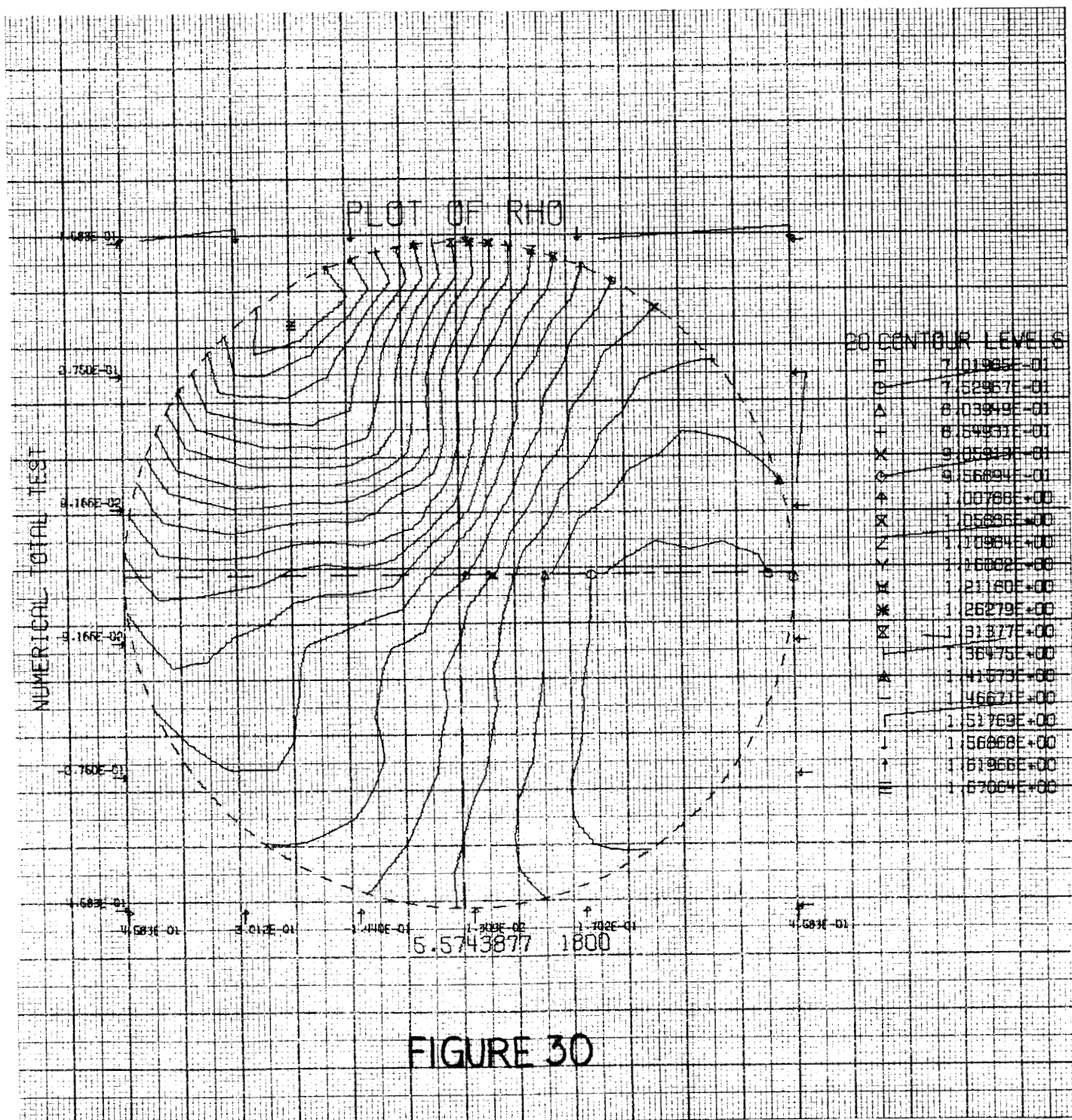
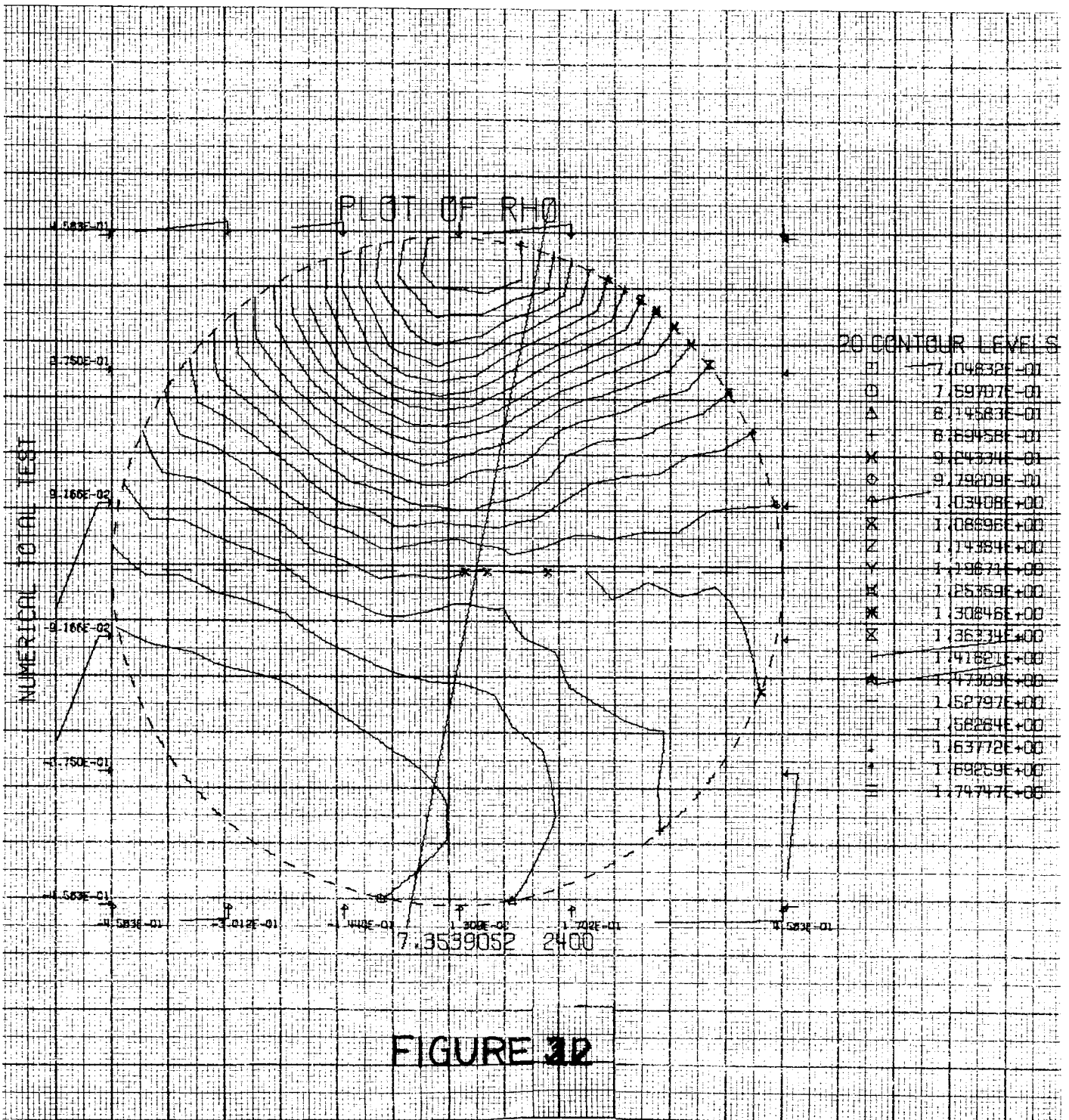


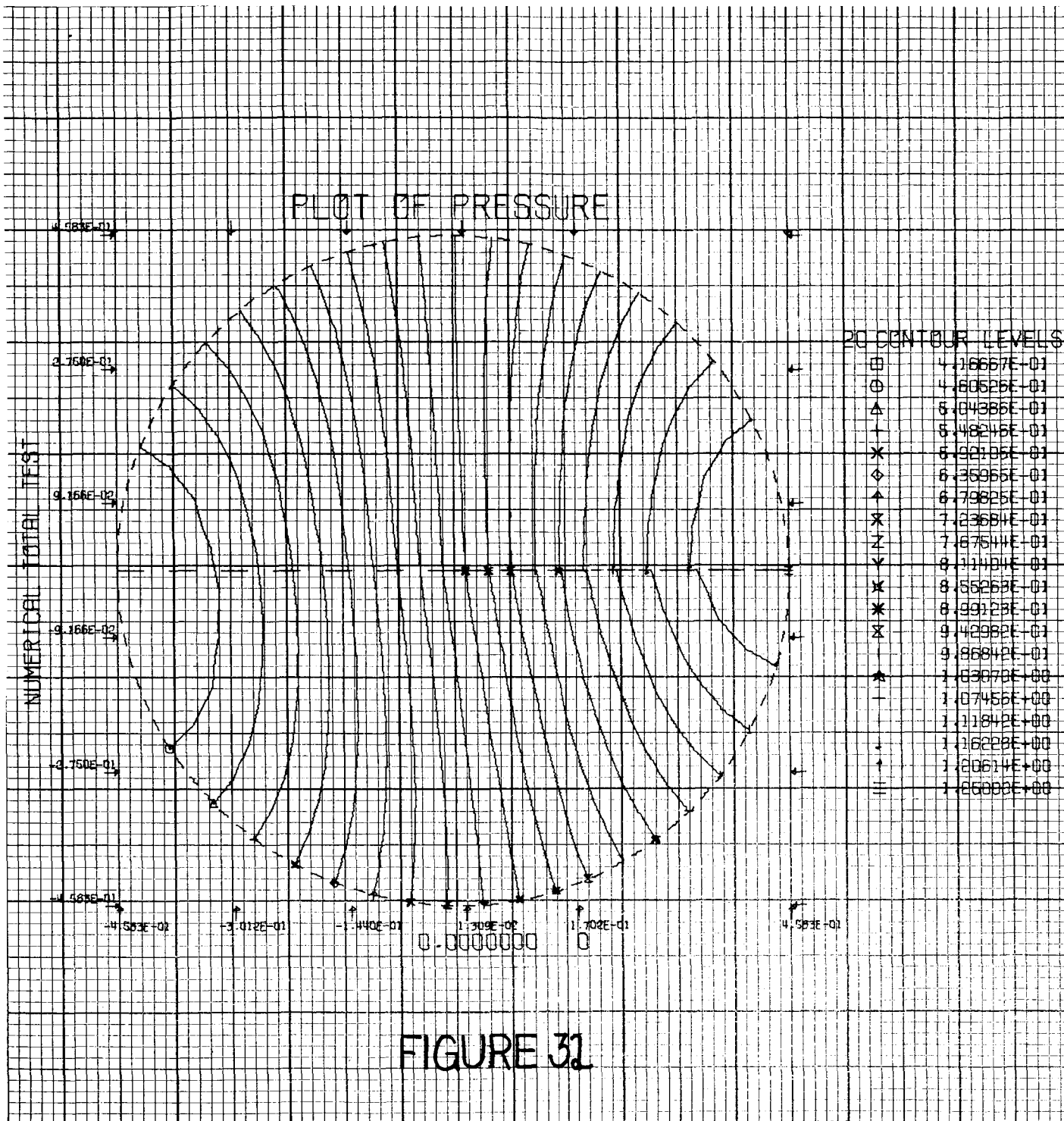
FIGURE 27

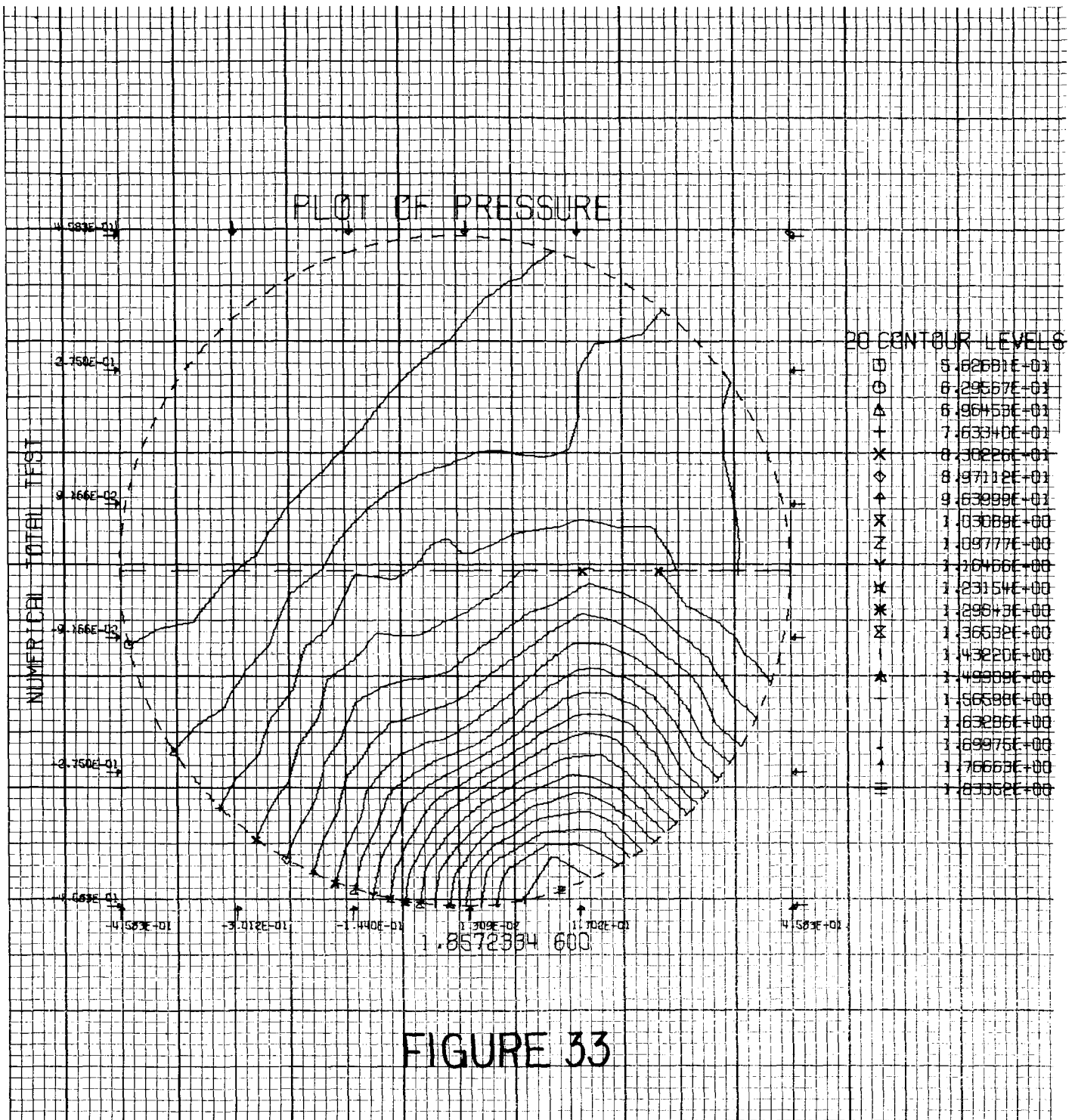


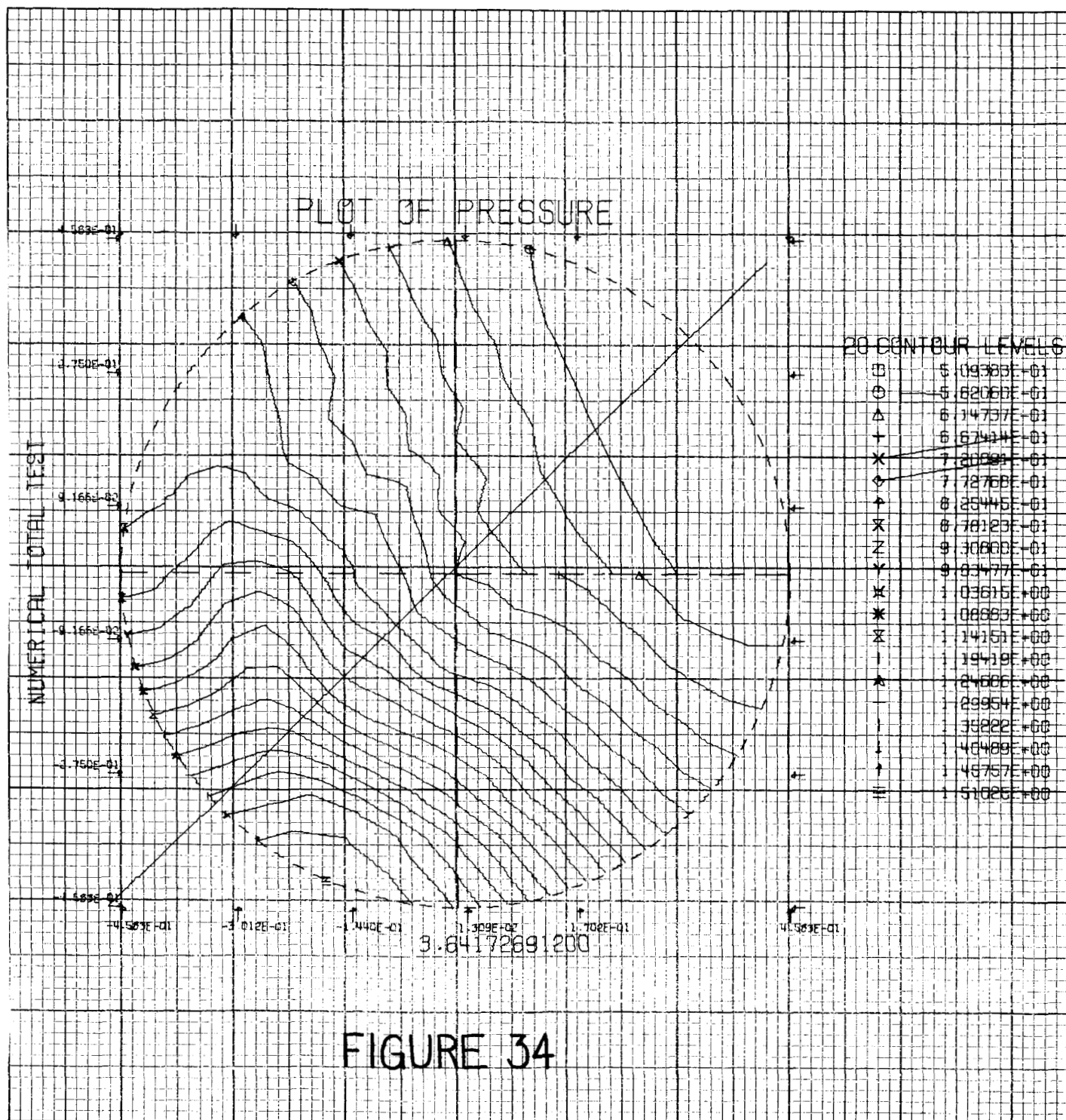


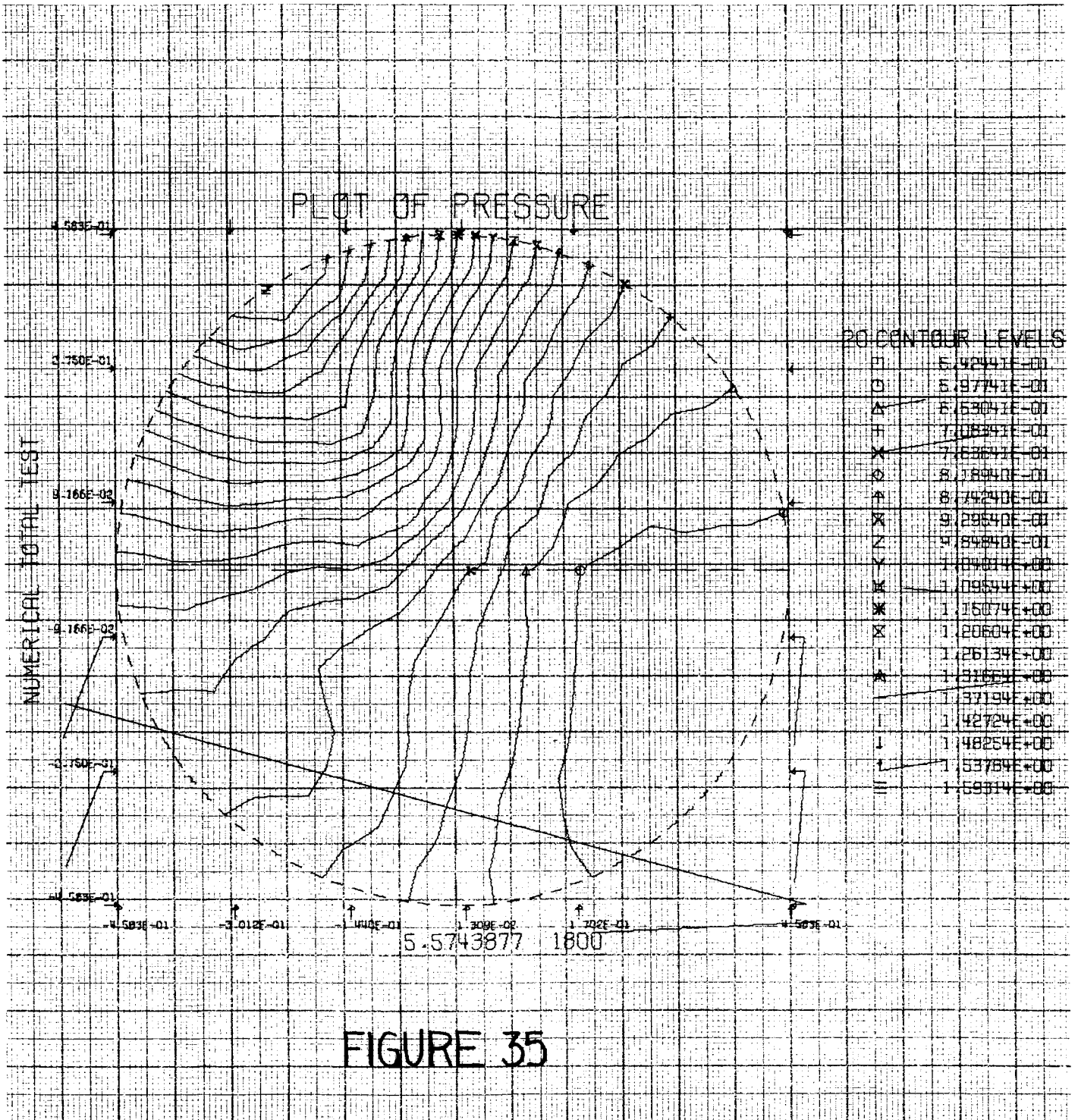


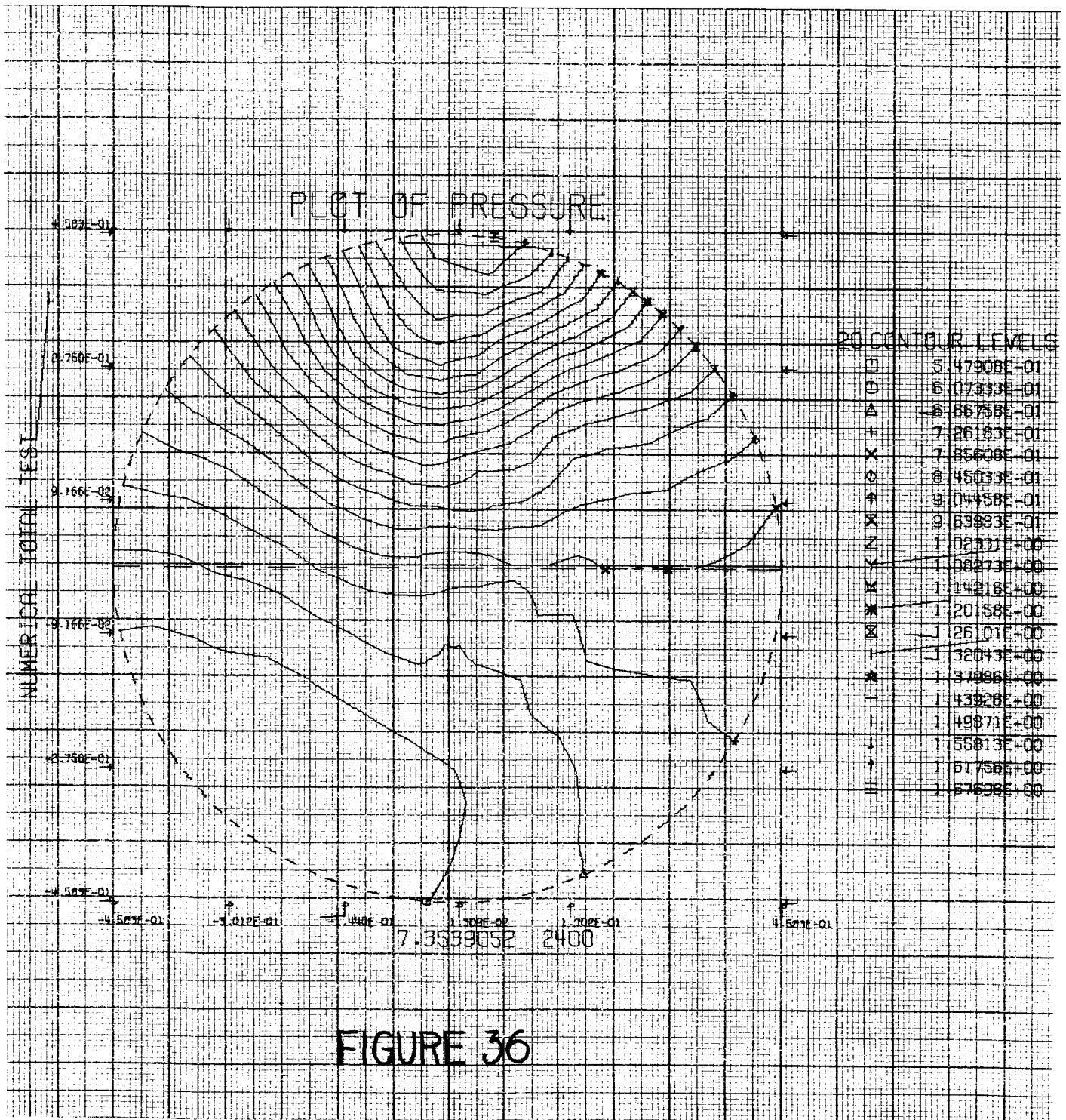


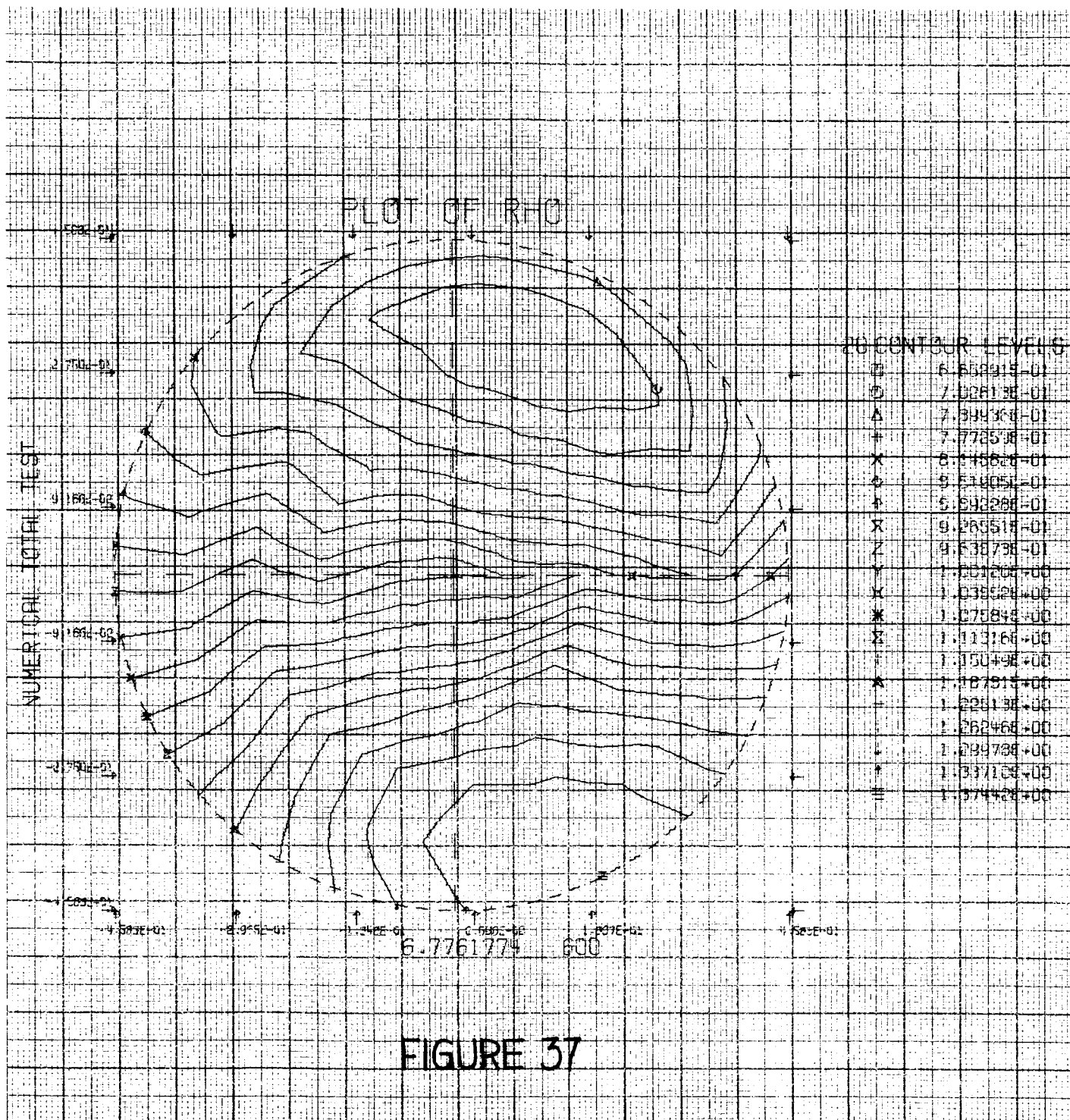


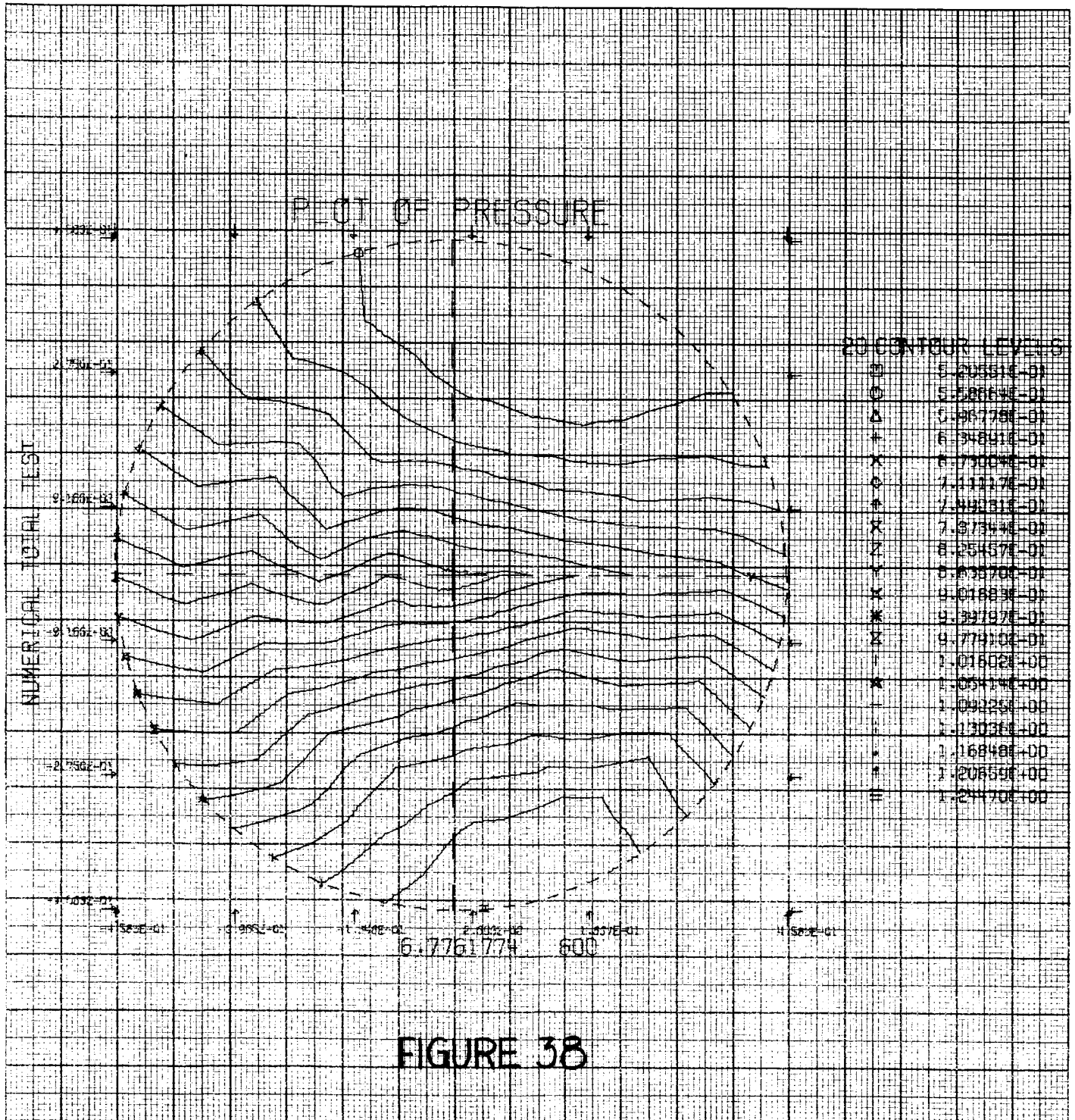






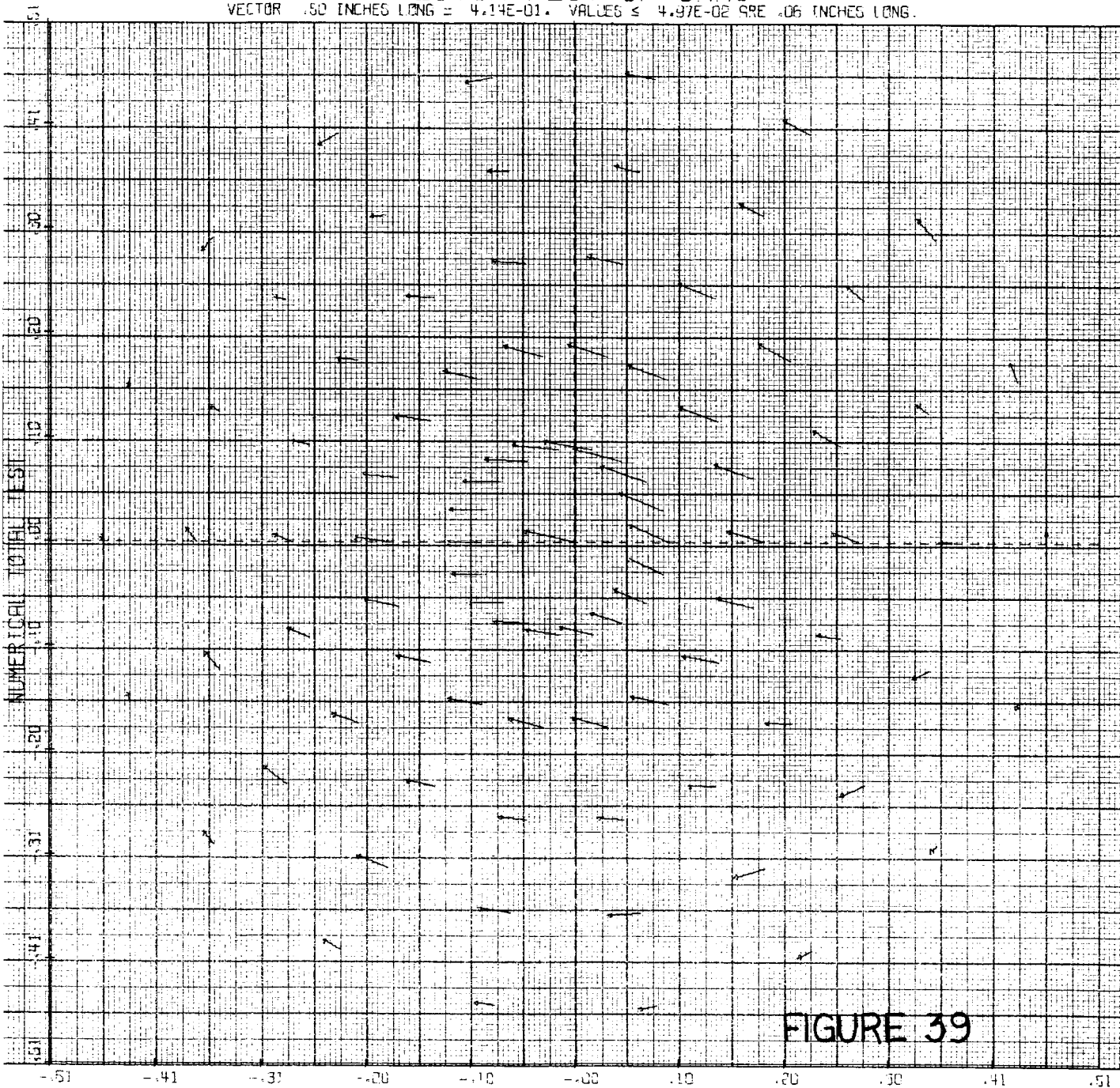




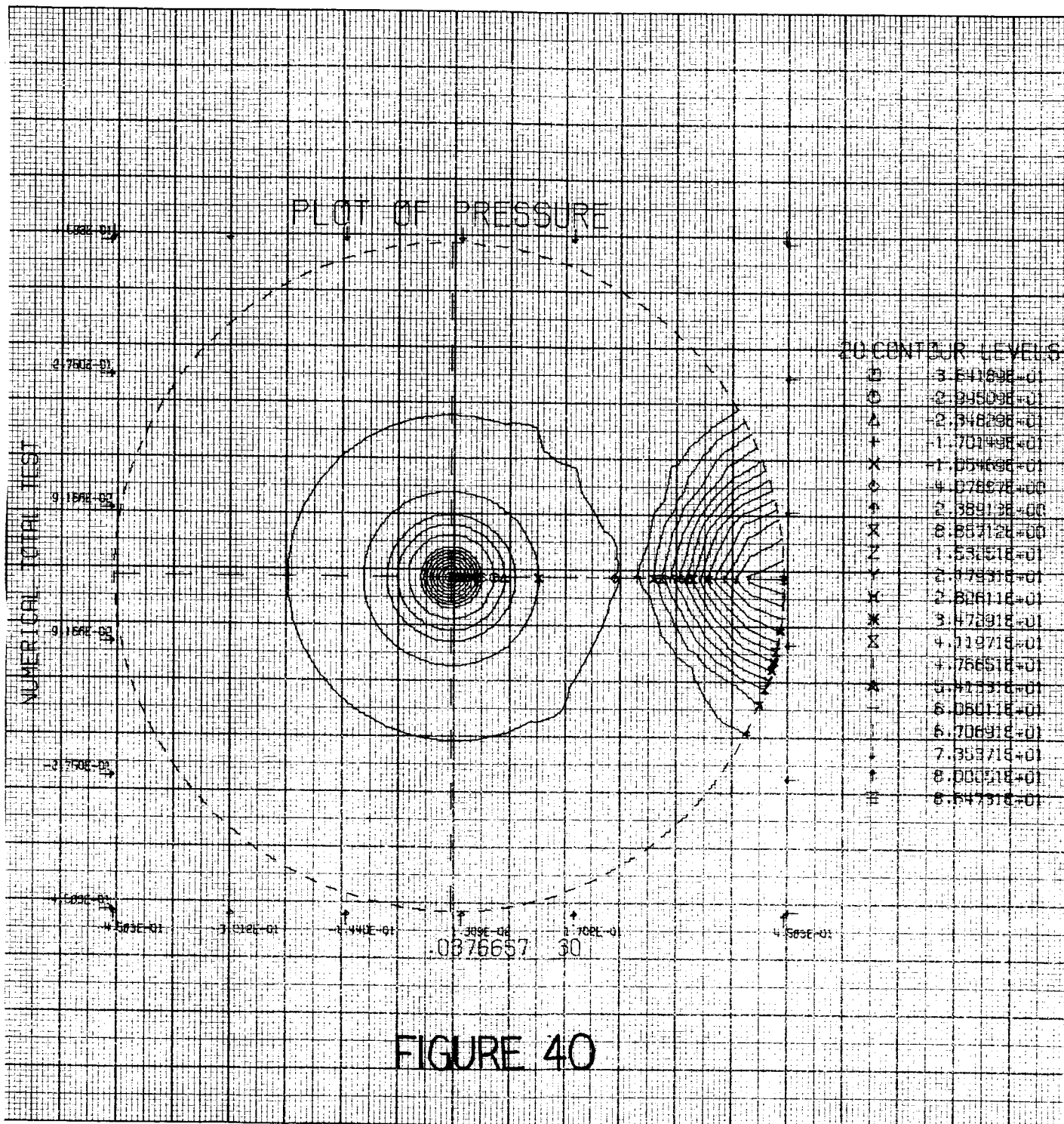


VECTOR PLOT OF UMAG

VECTOR .50 INCHES LONG = $4.14E-01$. VALUES $\leq 4.97E-02$ ARE .06 INCHES LONG.

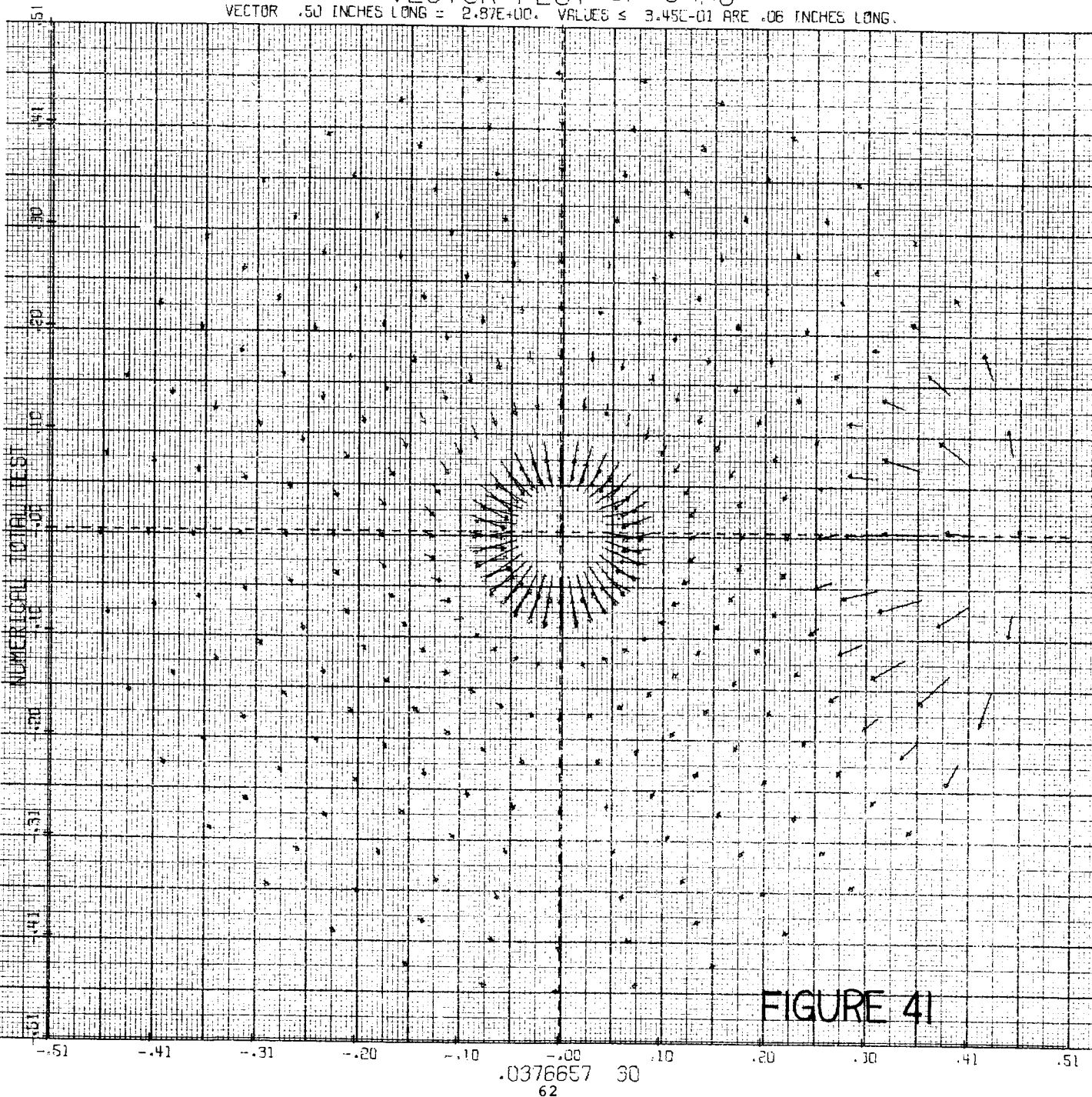


6.7761774 600



VECTOR PLOT OF UMAG

VECTOR .50 INCHES LONG = $2.87E+00$. VALUES $\leq 3.45E-01$ ARE .06 INCHES LONG.



REFERENCES

1. Burstein, S. Z. and Chinitz, W., "Nonlinear Combustion Instability in Liquid Propellant Rocket Motors", First Quarterly Report, Mathematical Applications Group, Inc., October 30, 1967.
2. Peskin, R. L. and Wise, H., AIAA Journal, 4, 1646 (1966).
3. Dynamic Science Quarterly Progress Report, "Combustion Instability and Random Wave Phenomena", Contract NAS7-467, SN-95, October 31, 1967.
4. Ibid, Monthly Status Report SN-95-4.
5. Dow Chemical Company, JANAF Thermochemical Tables.

APPENDIX A

Calculation of Nitrogen Tetroxide Equilibrium

Nitrogen tetroxide (N_2O_4) is assumed to decompose according to the following reaction equation:



Atomic conservation yields:

$$N: \quad 2 = 2a + b + c \quad (A.2)$$

$$O: \quad 4 = 4a + 2b + c + 2d \quad (A.3)$$

The equilibrium equations selected were:

$$N_2O_4 = 2NO_2: \quad K_1 = \frac{x_2^2}{x_1} p \quad (A.4)$$

$$NO_2 = NO + \frac{1}{2}O_2: \quad K_2 = \frac{x_3 x_4^{\frac{1}{2}} p^{\frac{1}{2}}}{x_2} \quad (A.5)$$

where x_i is the mole fraction of species i ($1 = N_2O_4$, $2 = NO_2$, $3 = NO$, $4 = O_2$), K_j is the equilibrium constant for reaction j , and p is the pressure.

Equations (A.2) - (A.5) are sufficient to solve for the four unknown species concentrations once p and T are specified. (It will be recalled that $K_j = K_j(T)$, and are obtained from Reference .) The Newton-Raphson iterative technique was employed to solve this system of equations.

The calculations yield the anticipated result that the concentration of N_2O_4 over most of the range of likely engine operating conditions is negligible. This accounts for its neglect in the chemical kinetic mechanism of Table II.

TABLE I

REACTION	ORDER	REACTION RATE CONSTANT
1) $\text{N}_2\text{H}_4 \rightarrow \text{NH}_3 + \frac{1}{2}\text{H}_2 + \frac{1}{2}\text{N}_2$	1	$10^{10.33} \exp \left(- \frac{36,170}{RT} \right)$
2) $\text{N}_2\text{H}_4 + 4\text{NO}_2 \rightarrow 6\text{NO} + 2\text{H}_2\text{O}$	2	$10^{15.83} \exp \left(- \frac{26,700}{RT} \right)$
3) $\text{N}_2\text{H}_4 + 2\text{NO} \rightarrow 2\text{H}_2\text{O} + 2\text{N}_2$	1	$10^{10.17} \exp \left(- \frac{39,600}{RT} \right)$
4) $\text{N}_2\text{H}_4 + \text{O}_2 \rightarrow 2\text{H}_2\text{O} + \text{N}_2$	1	$10^{9.91} \exp \left(- \frac{37,200}{RT} \right)$
5) $\text{NH}_3 + \frac{5}{2}\text{NO}_2 \rightarrow \frac{7}{2}\text{NO} + \frac{3}{2}\text{H}_2\text{O}$	2	$10^{15.85} \exp \left(- \frac{33,800}{RT} \right)$
6) $\text{NH}_3 + 3\text{NO} + \frac{5}{2}\text{N}_2 + \frac{3}{2}\text{H}_2\text{O}$	-	No Reaction
7) $\text{NH}_3 + \frac{3}{4}\text{O}_2 \rightarrow \frac{1}{2}\text{N}_2 + \frac{3}{2}\text{H}_2\text{O}$	2	$10^{14.61} \exp \left(- \frac{38,700}{RT} \right)$
8) $\text{H}_2 + \text{NO}_2 \rightarrow \text{NO} + \text{H}_2\text{O}$	2	$10^{21.5} \exp \left(- \frac{58,000}{RT} \right)$
9) $\text{H}_2 + \text{NO} \rightarrow \text{H}_2\text{O} + \frac{1}{2}\text{N}_2$	-	No Reaction
10) $\text{H}_2 + \frac{1}{2}\text{O}_2 \rightarrow \text{H}_2\text{O}$	1	$10^{10.96} \exp \left(- \frac{38,200}{RT} \right)$

• TABLE II

SPECIES GENERATION EQUATIONS

- (a) $R_1 = -\rho Y_1 \left(k_1 + k_2 \left(\frac{\rho Y_6}{M_6} \right) + k_3 + k_4 \right)$
- (b) $R_2 = k_1 \rho Y_1 \frac{M_2}{M_1} - \rho Y_2 \left(k_5 \frac{\rho Y_6}{M_6} + k_7 \frac{\rho Y_8}{M_8} \right)$
- (c) $R_3 = \frac{1}{2} k_1 \rho Y_1 \frac{M_3}{M_1} - \rho Y_3 \left(k_8 \frac{\rho Y_6}{M_6} + k_{10} \right)$
- (d) $R_6 = -\rho Y_6 \left(4k_2 \frac{\rho Y_1}{M_1} + \frac{5}{2} k_5 \frac{\rho Y_2}{M_2} + k_8 \frac{\rho Y_3}{M_3} \right)$
- (e) $R_7 = \frac{\rho Y_6 M_7}{M_6} \left(6k_2 \frac{\rho Y_1}{M_1} + \frac{7}{2} k_5 \frac{\rho Y_2}{M_2} + k_8 \frac{\rho Y_3}{M_3} - 2k_3 \rho Y_1 \frac{M_7}{M_1} \right)$
- (f) $R_8 = - \left(k_4 \rho Y_1 \frac{M_8}{M_1} + \frac{3}{4} k_7 \rho^2 \frac{Y_2 Y_8}{M_2} + \frac{1}{2} k_{10} \rho Y_3 \frac{M_8}{M_3} \right)$
- (g) $R_9 = 2 \rho Y_1 \frac{M_9}{M_1} \left(k_2 \frac{\rho Y_6}{M_6} + k_3 + k_4 \right) + \frac{3}{2} \rho Y_2 \frac{M_9}{M_2} \left(k_5 \frac{\rho Y_6}{M_6} + k_7 \frac{\rho Y_8}{M_8} \right) + \rho Y_3 \frac{M_9}{M_3} \left(k_8 \frac{\rho Y_6}{M_6} + k_{10} \right)$
- (h) $R_4 = \rho Y_1 \frac{M_4}{M_1} \left(\frac{1}{2} k_1 + 2 k_3 + k_4 \right) + \frac{1}{2} k_7 \rho^2 Y_2 Y_8 \frac{M_4}{M_2 M_8}$